IEEE Access
Multidisciplinary | Rapid Review | Open Access Journal

Received October 26, 2020, accepted November 14, 2020, date of publication November 26, 2020,
date of current version December 11, 2020.

Digital Object Identifier 10.1109/ACCESS.2020.3040895

Hydrofluoroether Impurities–Chemical Detection Using a Deep Learning Laser Speckle Contrast Evolving Spiking Neural Network

ALI SYARIATI MOHD SALLEH, HAZA NUZLY ABDUL HAMED, MOHD ADHAM ISA, AND HABIBOLLAH HARON
School of Computing, Universiti Teknologi Malaysia, Johor Bahru 81310, Malaysia

Corresponding author: Ali Syariati Mohd Salleh (alisyariatimohdsalleh@gmail.com)

This work was supported by the Ministry of Education Malaysia and Universiti Teknologi Malaysia through Fundamental Research Grant Scheme under Grant R.J130000.7851.5F069.

ABSTRACT Hydrofluoroether (HFE) impurities detection is an issue related to detecting chemical contamination within a high volume manufacturing (HVM) chiller caused by a rapid emulated environmental attack. The aftereffects of the cycle emulated attack may eventually create a micro-crack in the heat-exchanger. This event eventually causes the contamination of HFE due to multiple chemical interactions. This study proposes a new classification methodology to detect HFE chemical impurities using induction by a 532nm laser. The purpose of the laser induction is to leverage its laser speckle contrast attributes and amplify its detection. One of the reasons for choosing the 532nm laser spectrum is its highest quantum efficiency. Once amplification of detection is achieved, the detector tends to be in a highly sensitive mode due to low marginality to differentiate between two different conditions. This mode is prone to be stochastic. Thus, a new form of architecture known as Deep Learning Laser Speckle Contrast Evolving Spiking Neural Network (DL-LSC-ESNN) is proposed. The architecture utilizes speckle contrast domain conversion, dimensional additivity of the receptive neuron of evolving spiking neural network (ESNN), followed by the strength of Convolution Neural Network (CNN) feature extraction (FE) capability. Ultimately, the evolving and adaptive ability of ESNN is assimilated and integrated seamlessly. CNN acted to extract only an important spike train, and the result is its essences of important spikes or spike feature maps. The spike feature maps are then fed into the ESNN neuron repository, which either assimilates or creates a new neuron repository. The proposed methods show significant improvement in the accuracy of detection against multiple baseline state of the art CNN architecture and ultimately demonstrated its capability to detect real-time contamination of HFE thus improved the detection rate significantly for the HVM environment.

INDEX TERMS Hydrofluoroether, laser speckle contrast, high volume manufacturing, industrial chiller, ESNN, CNN, deep learning.

I. INTRODUCTION

Industrial chillers are used in a variety of applications in which a liquid is circulated through process machinery. In this case study, the chilled liquid is water from plant chilled water (PCW), the refrigerant agent is hydrofluoroether (HFE) with its coolant agent (lubricant oil), and the targeted cooling process is a central processing unit (CPU). This cooling mechanism is to simulate a temperature environmental attack via a temperature control into a central processing unit (CPU) die layer on a high volume manufacturing (HVM) enviroment. A HVM is known to be continually subjected to disturbance, which cause deviation and stachostical in nature [1], [2]. The disturbance of this stachostical are relatable to HVM's process monitoring [1] and tool variation [3], [4]. Even at optimal HVM preventive maintenance schedule to mitigate the risk of sudden failure a failure still occurs stachostically [5].

The core subjugated issue with HVM is that temperature changes are in rapid and continuous transformation.

The associate editor coordinating the review of this manuscript and approving it for publication was Guijun Li.

This leads to a phenomenon known as the kinetic theory of matter [6]–[10]. Under this rapid continuous transformation, microcracks are induced in the heat exchanger coil which creates an environment in which a mixture of chemicals is induced. The interconnection between these media eventually creates an environment where HFE and lubricant oil are forcefully combined. Thus by this effected conditioning, a pseudo mixture of these two chemicals within the heat exchanger eventually lead to CPU stain that ultimately contributed to the elimination of the CPU. Further investigation of the microcrack environment indicated that the contamination is in low sensitivity due to the inadequate amount of interconnection between these two chemicals. Thus an amplification and the pre-detection system are needed to assist and triggered if the microcrack environment happened and eventually leads to a robust detection system with the usage of lasers both as a light source and for detection amplification.

The detection methodology and its image capturing system deployed in HVM environment uses a hybrid technique of Particle Image Velocimetry (PIV) [11] and Dynamic light scattering (DLS) [12]. PIV is most commonly used as a quantitative method that able to measure the particle velocity on spatial and temporal domains relative to the planar or tomographic dimension [13]–[15]. References [13], [14], and [15] also mentioned the application of PIV-CNN on estimating a dense motion field which able to provide details (small-scale structures) of the turbulence flow. Reference [13] architecture starts by inputting a particle image pair and the output is a velocity field with displacement vectors at every pixel which provides a final reconstruction of particle image rather than a pure classification. While [14] architecture focuses more on regression-based PIV estimator rather than a classifier. Reference [15] applied an architecture that able to determines the likelihood of each area containing focused particles in the re-projected 3D image stacks that recreate and forecasted the velocity under the influences of flow field reconstruction. A DLS uses the recording of the fluctuations in scattering intensity overtime to characterize motion within the sample [16]. By quantifying these fluctuations, through either correlation or spectral analysis, diffusion coefficients can be calculated which in turn can be used to determine the hydrodynamic properties. In short, DLS measures how scattering changes over time, regardless of the amplitude of detection. This fundamental principle is further explained by [17]. In [18], the research emphasis is on predicting fluids containing nanoparticles and microparticles against the traditional DLS process. Reference [18] described the challenge and the objective of the stochastic process was to be generated using a deterministic method, the time series provided by consistent light scattered by a suspension. The research results concentrate on proof of concept using neural networks (NN) for the processing of DLS time series. Research in [19] approach of light scattering control to determine the functional relationship between transmitted and reflected speckle patterns using NN. In [20], the utilization of SVM is to predict the holographic conditioning of colloidal spheres which aligned with Lorentz-Mie theory that enables it to track each particle in three dimensions and measure its size and refractive index. Conclusively, PIV usability was focalized in a randomness repeatable motion via its statistical properties measurement which eventually contributed to its velocity attributes [21]–[23] whereas DLS acted as a backbone application for the fundamental of detection of a particle in static liquid form [17].

The basic foundation of HFE impurities detection can be described by imaging a condition where a laser hits the container (polycarbonate transparent coupler), the coupler is illuminated with a laser source, the scattered light yields a speckle pattern in the far-field. Thus the lightning distribution is by default consistent. All of the molecules in the HFE are being hit with the light and all of the molecules diffract the light in all directions [12]. The diffracted light from all of the molecules can either interfere constructively (light regions) or destructively (dark regions). The stochastical element described is the velocity in liquid form which being constantly bombarded with diaphragm pump fins. This to mimic quick and transformative chemical reactions between these two chemicals.

Ultimately both techniques focalize on detecting the stochastic behavior of the particle using a laser as main source illumination. This is due to the nature of detection, which is stochastic, eccentric and unpredictable. As stated by [24], the illumination with a laser source eventually scattered light yields with a speckle pattern. The speckle pattern is the property that eventually is harnessed to amplify the chemical contamination detection.

Due to the condition of HVM, which is stochastic by nature, a new architecture known as deep learning laser speckle contrast evolving spiking neural network (DL-LSC-ESNN) is introduced. The DL-LSC-ESNN utilizes CNN for its feature extraction layers. This is due to CNN's ability to represent its input as a tensor in which local elements are correlated with one another [25].

The nature of HVM HFE contamination is highly erratic in its random particle displacement. To combat this a computational model is needed to capture and learn the whole patterns from data streams to more accurately predict future events for new input data. The brain-inspired ESNN has the ability to learn patterns using trains of spikes [26]. Furthermore, the 3D topology of a spiking neural network (SNN) reservoir has the potential to capture an entire pattern at any given time point [27]. This feature is a focal requirement and eventually leads to the choosing of ESNN architecture. A further characteristic of ESNN, as stated by [28], is that it can quickly adapt the new knowledge. The system performs dynamic adaptation to its synaptic weight either by assimilating similar information or creating a new synaptic weight repository [29]. Thus, this study will investigate and explore a highly robust mechanism for adaptability and evolving ability, eventually leadings to an image classification technique with the core combination strength of CNN (spike features extraction) and evolving ability of ESNN.

II. MONOCHROMATIC POLYCARBONATE LASER ATTRIBUTES

This study experimented with the HFE laminar flow. As the HFE within the cylindrical polycarbonate containment chamber occurs when the laser hits the polycarbonate transparent coupler; the coupler is illuminated with a laser source, the scattered light yields a speckle pattern in the far-field. The spatial intensity distribution of speckles is dictated by the summation of the angular-dependent scattering efficiencies of the density fluctuations in the illumination/detection volume and by the phase relationship of the scattered fields [24]. Thus, the lightning distribution is by default consistent. All of the liquid molecules in the HFE polycarbonate chamber are hit with the light and all of the molecules diffract the light in all directions [12]. The diffracted light from all of the molecules can either interfere constructively (light regions) or destructively (dark regions). As in liquid form, light delays its traverse time, thus creating a pseudo-event of light absorption [12].

Further investigation of this study indicated that a laser speckle pattern is generated on the rough surface by laser irradiation, and the laser speckle particles relate to the laser wavelength and sample surface roughness and have a more standardized distribution [30]. To simplify the attribute dependencies, laser speckle is not directly influenced by temperature and is thus appropriate for the measurement of deformation in an extremely high-temperature setting that may compensate for the exclusion of artificial speckles. Here. the temperature can be excluded as not a dependency.

The correlation of the speckles which pass through a dynamic scatter was studied by [31], who found that this feature is related to the structure of the surface of scatter and laser coherence [32]. As the speckle pattern dependencies is on its surfaces, impurities in the HFE smart coupler designed with polycarbonates has to go through a process control to maintain its surface consistencies. Reference [33] mentioned that coherence for laser beams passing through a movement diffuser is based on the period of time of observation; time coherence and spatial coherence were considered. Speckle noise can obviously be caused by a spatially incoherent laser light source [34]. This can be countered by using a control mechanism to capture the laser images through a smart feedback system.

Over the years, the study of speckle was delineated by speckle contrast (SC) which was defined as the relationship of the standard deviation between intensity fluctuation and mean intensity. The fact that SC has a clear physical meaning and is mathematically convenient makes it appealing. SC varies according to changing mean intensity [35]. If translated by the similarity approach, the comparison is similar to the contrast representation.

Further research has indicated that the SC is supported by point spread function (PSF) tuning technique as a countermeasure. Due to its essential deconvolution processing and retrieving the object's image [36], the PSF polarization is implemented, as it has proven useful for imaging targets in dispersing media and for enhancing the contrast of images [37]. Ultimately, the path indicated that a monochromatic lasers are subdivided into three categorical approaches: irradiation, coherence and randomize phases. Each categorical can be translated into a speckle contrast core attributes which are subdivided on two categories of fluctuation and mean intensity.

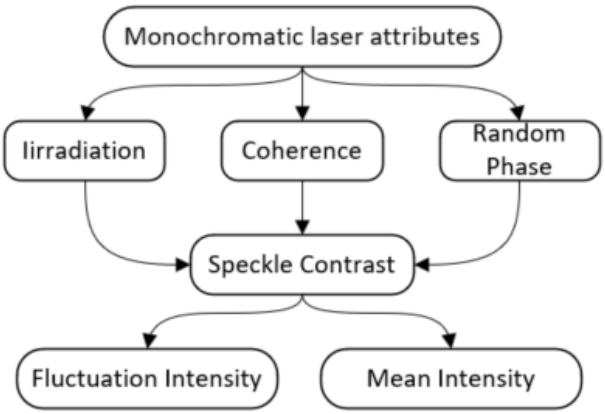

FIGURE 1. Flow of monochromatic laser attributes.

Further investigation for the study as per observed indicated that either mean or fluctuation intensity are not completed without proper representation via an encoding technique. This is due to the encoding will represented the information in much deeper and different perspective.

Fig. 1 shows the attributes of monochromatic lasers that will be used to encode the laser from its original images with SC properties, using the mean intensity approach [38] to spike train encoding of rank order population (ROP) by [39]. The encoding approach is to amplify the spike train domain before FE layer. This ensures that only the strongest essences of spike are captured and represented on the final FE before being fed into the ESNN layer.

The laser image will be divided into nine sections. Referring to Fig. 2, each section represent contrast attributes. Fig. 2 section 1, 3, 4, 5, 6, 7 and 9 heavily align with SC concept. Fig. 2 section 2 and 8 shows heavy contrast and brightness intensity. These attributes will be further encoded with the encoding scheme. This is to boost its dimensional additive.

A. QUANTIFICATION AND FORMULATION OF MONOCHROMATIC POLYCARBONATE LASER SPECKLE CONTRAST ENCODING

Laser Speckle Contrast Imaging (LSCI) is a sophisticated and useful imaging method that uses the speckles of a highly coherent light source (laser source), that are randomly generated on the image sensor. This imaging technique is regarded as an economical method to obtain information on the movement or flow of the target medium [38].

The speckle contrast can be determined by analyzing the reflection intensity of the image [38], [40]–[43]. The speckle

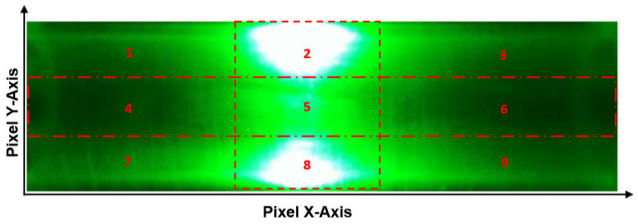

FIGURE 2. Impurities HFE polycarbonate sectional analysis.

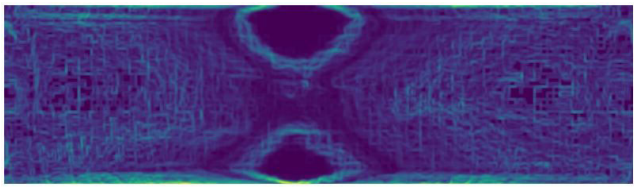

FIGURE 3. The SC mean intensity 5 × 5 windows conversion.

contrast, K, can be calculated using Equation (1).

$$K = \frac{\sigma_{std}}{\langle I \rangle} \tag{1}$$

In Equation (1), K represents the speckle contrast, σ_{std} is the standard deviation, while $\langle I \rangle$ is the mean of the intensity of the reflectance image in a region of interest (ROI). The raw images (1920 × 1080 with original 96dpi) were first interpolated by resizing it to (800 × 680 with default 96dpi) to reduce the computational cost [44], [45] and also due to limitation of resources [46]. As mentioned by [47], the resizing has minimal impact upon resolution loss. The resized image array of 800 × 680 pixels is split into 5 × 5 pixel windows in this experiment prior to computing the SC. Consequently, the ROI of 25 pixels in the initial images is converted into one pixel and the lateral laser speckle image pixel size is decreased by five times compared to the raw image. Fig. 3 is the conversion result from normal RGB to SC mean intensity using the 5 × 5 window.

As for the spike train encoding, this study utilizing ROP. The ROP is being chosen due to drawbacks of conventional spiking neural network (SNN) long simulation rate coding probabilistic conversion [48]. The ROP is proposed to alleviate this issues by encoding the SC images to pixel-based spikes. Further justification of this conversion process is the requirement to comply to ESNN usability. From a biological perspective, as the retina cells fire with remarkable temporal precision [49], a single spikes can, in principle, carry substantial information about visual stimuli [50]. Extensive justification indicates that the underlying idea behind ROP is that individual cells by themselves do not carry much information, but together, as a population, they are or could be sufficient. Reference [51] suggests that in synergistic encoding of information in the relative activities of a neuronal population is a feature of the retinal ganglion cells (RGC) responses at the population level. This observation indicates the effectiveness of applying ROP-based encoding, which in reality nearly emulates nature. The spiking encoding scheme accomplishes an information ventral stream. This means that both spiking rate and time can be used to represent the structural information within ventral stream. As the intensity of a stimulus increases, the rate of spikes increases to convey much more important information [52]. To summarize, the ROP true functionality is its ability to generated spikes by sequentially sorting input values from its pre-layers [48] after SC conversion.

Aforementioned the input information must be expressed in spikes in ESNN, Fig. 3 's conversion image must be encoded in spikes. ESNN is well known to be encoded in ROP encoding scheme. The ESNN encoding scheme requires the real valued dataset to be mapped into a sequence of spikes. To achieve this, a neural encoding technique is required. The ESNN utilizes ROP encoding as its encoding scheme. This technique was first described by [53]. Receptive fields allow continuous values to be encoded using a set of neurons with overlapping sensitivity profiles. Each input variable is represented independently by one dimensional receptive field unit M. For variable n of the interval $[I_{min}, I_{max}]$ is defined. The Gaussian receptive field (GRF) of neuron j is given by its center C_j.

$$C_j = I^n_{min} + \frac{2_j - 3}{2}\left(\frac{I^n_{max} - I^n_{min}}{N - 2}\right) \tag{2}$$

And with W_j width:

$$W_j = \frac{1}{\beta}\left(\frac{I^n_{max} - I^n_{min}}{N - 2}\right) \tag{3}$$

With $1 \leq \beta \leq 2$. Parameter β controls the width of Gaussian receptive field. The output of neuron j is defined as:

$$output_j = exp\left(-\frac{(x - C_j)^2}{2W_j^2}\right) \tag{4}$$

where x is the input value. The firing time of each pre-synaptic neuron j is defined as:

$$T_j = \left|T(1 - output_j)\right| \tag{5}$$

Ultimately the enhanced process of introducing the laser properties ROP encoding produced a higher dimensional visibility of laser image representation as compared to conventional RGB representation. The laser image is represented via a spike configuration. A spike as in its raw form can carry substantial information about visual stimuli [50]. This representation can be expanded as in the analogue form of amplitude, phase and frequency. Thus, it may provide boundless visibility to further conjecture how the spike functions.

III. CONVOLUTION NEURAL NETWORKS (CNN)

In the last few years, CNN has become an outstanding technology and has led to better performance in many fields. A CNN architecture has several iterative levels, including convolution, ReLu, and pooling layers. This layer is ostentatious, but non-linear [54]. The difference is that the importance of feature extraction layers is emphasized by CNN.

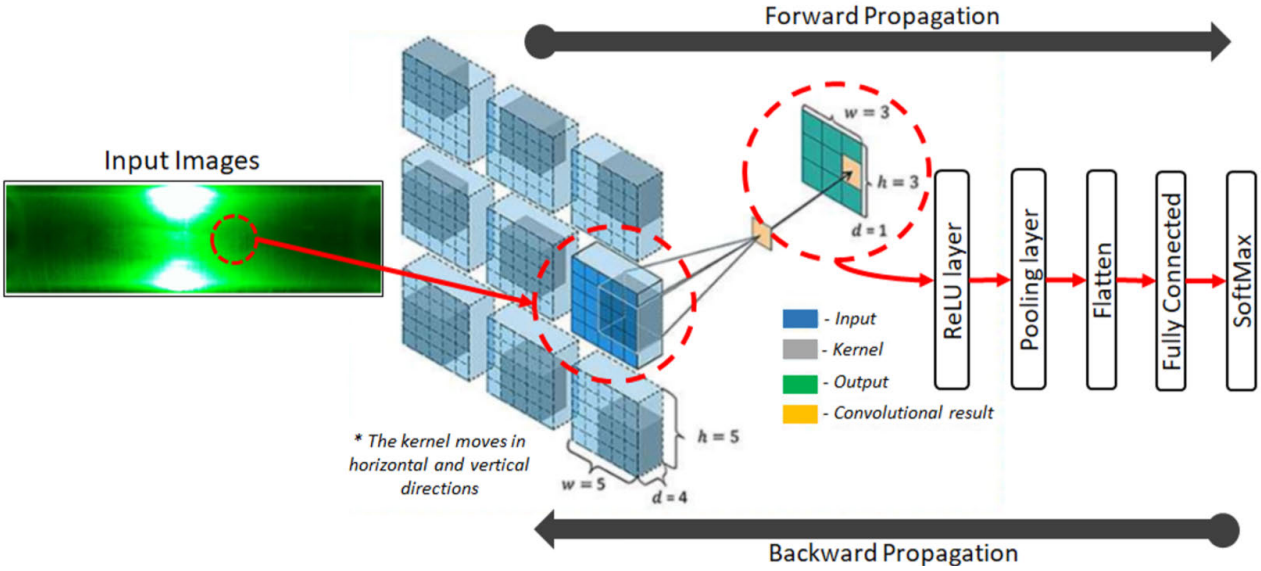

FIGURE 4. Conventional CNN with forward and backward propagation flow. Iterative layer of convolution, ReLu and pooling are being utilized for FE.

To put into perspective, input representation in a low level can be transformed by each layer into an abstract representation.

IV. SPIKING CNN

A typical Spiking CNN consists of CL, PL, a fully connected linear classifier, and a spike counter. Its follow conventional CNN in the same order except the existence of spike counter. As the CL uses weight sharing to reduce the number of parameters as in a conventional CNN. The information in a spiking CNN is transferred via spike trains instead of real values [55], [56]. The spike train conventional generated via rank order or population based [48]. This to ensure that the neurons in CL detect more complex features by integrating input spikes from the previous layer which detects abstract visual features. The convolutional neurons emit a spike as soon as they detect their preferred visual feature which depends on their input synaptic weights [55], [57]. For each neuron is selective to a visual feature determined by its input synaptic weights on its specific map to detect the same visual feature but at a different locations. To this end, synaptic weights of neurons belonging to the same map should always be the same. As for the PL provide translation invariance using maximum operation, and also help the network to compress the flow of visual data [58]. Neurons in PLs propagate the first spike received from neighboring neurons in the previous layer which are selective to the same feature [57], [58]. The Spiking CNN's CL and PL are arrange in consecutive order if the magnitude of FE is needed further. Fig. 5 shows the network architecture of a typical spiking CNN.

Ultimately the justification from Spiking CNN indicated that the CL are significant due to its ability to extract only important spike generated after ROP conversion [48], [58]. Each CL extracts features through spiking convolution process. Then, the pooling layer combines the outputs of neurons

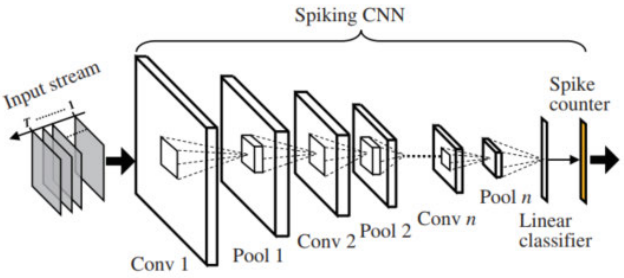

FIGURE 5. Typical network architecture of spiking CNN [58].

cluster in one feature maps (FM) into the input of one neuron in the next layer [58]. Pooling layer (PL) also behaves as a FM reducer by reducing the size of the FM by pooling maximum amplitudes given by CL [48].

A. QUANTIFICATION AND FORMULATION OF CNN

The CL is parameterized by the size and number of maps, the size of the kernel, the skipping factors, and the connection table. Each layer is similarly sized with M maps (*Mx, My*). A kernel (blue rectangle in Fig. 6) of size (*Kx, Ky*) is relocated over the appropriate region of the image input (i.e. the kernel must be inside the image completely). The *Sx* and *Sy* skipping factors determine how many pixels the filter / kernel skips between subsequent convolutions in x and y-direction [59]. The size of the output map is then defined per Equation (6):

$$M_x^n = \frac{M_x^{n-1} - K_x^n}{S_x^n + 1}; \quad M_y^n = \frac{M_y^{n-1} - K_y^n}{S_y^n + 1} \tag{6}$$

where index n indicates the layer. Each map in layer is connected to at most map in later. Neurons of given map share their weight but have different receptive fields.

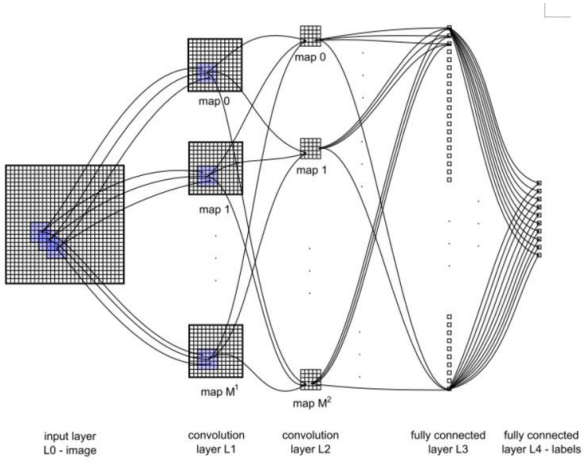

FIGURE 6. Architecture of convolution neural network [59].

The interpretation of Equation (6) can be compared to Equation (7a). Where the M is M maps or layers of images, s is the skipping factor or padding and K is the kernel or filters. B is bias.

$$Convolve_{\mathrm{a,b,c}} = \sum_{\mathrm{l=0}}^{\mathrm{k-1}} \sum_{\mathrm{m=0}}^{\mathrm{w-1}} \tag{7a}$$

$$\sum_{\mathrm{n=0}}^{\mathrm{h-1}} M_{\mathrm{sp+n,sq+m,r}} K_{\mathrm{lmn}} + B_{\mathrm{lmn}} \tag{7b}$$

For Equation (7a), the $Convolve_{a,,b,c}$ is the dot product of a representation of the summation of single M. For each M maps depth k, and for every width w of M on every height h, perform kernel multiplication K_{lmn} added with bias B_{lmn}. Fig. 6 shows the map representation from it nominal input layers L0, moves to convolution layer L1 map M^1 to convolution layer L2 map M^2. Each layer represents the dot product of each input representation.

The activation layer, consists of several activation functions. The activation functions include sigmoid, tanh and ReLu. Nowadays, the activation layer is typically ReLu, which from a mathematical perspective converts any non-zero to zero and linear to all positive values. Due to this, it is computationally cheap. Moreover, ReLu does not converge faster, as it does not suffer the vanishing gradient compared to sigmoid and tanh. In a sparse network, it is more likely that neurons are actually processing meaningful aspects of the problem. ReLu activation is referred to in Equation (8).

$$f(x) = \begin{cases} 0 & for\ f(x) < 0 \\ f(x) & for\ f(x) \geq 0 \end{cases} \tag{8}$$

A PL always is added after the CL. In general, the FM have been generated by a CL after a non-linearity (e.g. ReLU) had been applied. The pooling requires the choice of a pooling operation, similar to a filter for FM. The final size of the filter or pooling operation is always smaller than the size of the FM by a division of two. The pooling main objective is to reduce its FM by applying its function. The most commonly used pooling function is max pooling, as stated by Equation (9a).

$$f(x')_{d,e,f} = \max_{a,b \in P_{i,j}} f(x)_{a,b,c}, \tag{9a}$$

$$P_{i,j}\ is\ the\ window\ for\ Pooling\ operation \tag{9b}$$

V. EVOLVING SPIKING NEURAL NETWORK

The emerging ESNN [60], are definitely appealing in the context of HFE chemical contamination. An ESNN can grow and learn new information by evolving (e.g. adding) neurons without retraining it [61]. ESNNs function on-line by design, and ESNNs are given a quick updating and functional framework for adaptive online learning. This unique feature gives them the greatest benefit [62].

The above-mentioned developments in the use of large amounts of HFE data for online forecasts pose significant challenges linked to its stochastic character and its evolution over long periods [63], [64]. Without explicit specific plant models, ESNN's most obvious advantage is that its neural networks can learn to carry out satisfactory tasks. In circumstances in which identical copies are hard to find, this is strongly favored [65].

ESNNs are modular decentralized-based systems that continuously, independently coordinate, on-line, adaptively, evolving, and interactively build their structure and functionality on the basis of incoming information [28]. Its topology is purely feedforward, arranged in several layers, and the relations between the neurons of existing layers are subject to changes in weight. Based on the evolution and the topology, for a complex and unpredictable nature of HVM, an extensive version of ESNN is needed. As mentioned earlier, an ESNN by nature has the ability to evolve its neuron repository. The evolving nature is a key element of its success, as discussed [28], [66]. The purpose of the learning method is to generate output neurons, each of which is marked with a class label. The number and value of class labels depend on the classification problem to solve. The learning algorithm generates successively during the presentation of training samples a pool of trained output neurons. The idea is a single repository is evolved for each class label.

A. QUANTIFICATION AND FORMULATION OF EVOLVING SPIKING NEURAL NETWORKS

ESNN originated from the Evolving connectionist systems (ECoS) methodology, it was initially proposed by [61], and the architecture was intended to be used in visual pattern recognition [60]. From the perspective of a neural model, fundamentally it used a Leaky Integrated-and-Fire (LIF). This model was described by [67], as the information transfer is in spike domain. It describes the spike response as dependent upon arrival time. The early spike response is important due to the fact that the post-synaptic potential on the earlier spike is critical. This principle is fascinating because the brain is able to quickly and accurately measure even complex tasks using the information provided by these early spikes.

These early spikes generation fully utilizing the dynamism of Thorpe and Gautrais model are describe by dynamic of the

post-synaptic potential *ui(t)* of a neuron i:

$$ui(t) = \begin{cases} 0 & If\ fired \\ \sum_{j|f(j)<t} w_{ji} m_i^{order(j)} & Otherwise \end{cases} \quad (10)$$

where is the weight of a pre-synaptic neuron *j*, *f(j)* is the firing time of *j*, and $0 < m_i < 1$ is a parameter of the model, namely the modulation factor. Function *order (j)* represents the rank of the spike emitted by neuron *j*. For example, if *j* is the first among all pre-synaptic *i neurons* to emit a spike in the rank *order (j)* = 0. In a similar fashion, the spikes of all pre-synaptic neurons are ranked and then used in the computation of *ui*. A neuron *i* produced a spike if it exceeds a certain level of 0. After emitting a spike, the potential resets to *ui* = 0. Each neuron is allowed to emit only a single spike at most.

As for the learning methodology of ESNN, it used the algorithm from [66]. ESNN algorithm is an equivalent to feed forward and organized in multiple layers. The objective of the ESNN's learning method is to create output neuron, each with its own class label $I \in L$. Below is the equation used in the training algorithm.

$$w_j^{(i)} = (mod)^{order(j)}\ \nabla j | j\ pre - synaptic\ neuron\ of\ i \quad (11)$$

$$\gamma_i = PSP_{max(i)}.C \quad (12)$$

$$PSP_{max(i)} = \sum j w_{j,i} mod^{(j)} \quad (13)$$

$$W_{j,i} = \frac{w_{new} + (w_{j,i}.M)}{M+1} \quad (14)$$

$$\gamma_i = \frac{\gamma_{new} + (\gamma_i.M)}{M+1} \quad (15)$$

These early spikes generation fully utilizing the dynamism of Thorpe and Gautrais model are describe byEquation (11) to Equation (13), and indicate the relation between the pre-synaptic neuron j and the neuron generated *i*. Parameter *mod* is the modulation factor of the Thorpe and Gautrais neural model. Different labelled output neurons may have different modulation factor *mod*. The function *order (j)* represent the rank of the spike emitted by neuron *j* is the maximal possible potential of $\mathbb{R}\{0 < C < 1\}$.

Equation (14) and Equation (15) compare the trained neuron with the stored neuron in repository. If the Euclidean distance is smaller than (SIM), the trained output neuron is considered equivalent. As a result, the thresholds and weight vectors are assimilated according to Equation (14) and Equation (15) respectively. The merging uses an averaging of the connection weights and the average of two firing threshold. The merging will eliminate the trained neuron *i* and the next sample is processed. If no similarity is found as compared to trained neuron *i,* the neuron *i* is added to the repository as a new output neuron.

VI. PROPOSED DEEP LEARNING LASER SPECKLE CONTRAST EVOLVING SPIKING NEURAL NETWORK (DL-LSC-ESNN)

Due to the stochastical state of HVM, a new DL-LSC-ESNN architecture is proposed. As the core issues of the essence of HVM HFE contamination are highly unpredictable in random particle displacement in its laminar flow. To counter this a computational model must capture and learn all the trends from data streams in order to predict the most probable future events for new input data. One of DL-LSC-ESNN known components of ESNN has the ability to learn patterns by using ROP spikes [26] and is supported by a reservoir that has the potential to capture a whole pattern at any given time point [27]. ESNN, as described by [28], can quickly adapt the new knowledges by performing a dynamic adaptation to its synaptic weight [29]. Other components from the proposed DL-LSC-ESNN such as SC conversion at the input stages exist as a method to amplify the detection. As discussed, the SC conversion idea came from the fundamental of LSCI. The outcome of the investigation of this LSCI shown that the properties of laser speckle pattern generated on the rough surface of polycarbonate by laser irradiation, and the laser speckle particles relate to the laser wavelength and sample surface roughness have a more standardized distribution [30]. This eventually leads to straight forward and highly economical methodology to obtain the information on the laminar flow inside the polycarbonate chamber. This put the LSCI in the position of being harness as part of SC formulation and quantification. As for the CNN component integration with DL-LSC-ESNN, the integration aforementioned argument is on its reliable FE performance. CNN's FE ability together with SC's ROP integration eventually lead to tougher translational invariances immunity [58]. This distinctive ability and performance leads to the combination of all component and strengthens DL-LSC-ESNN adaptability to stochastic nature of HVM.

DL-LSC-ESNN architecture input starts by receiving the default image state in RGB format. The first step is the RGB conversion to SC domain. Next the SC domain conversion to grayscale pixel intensity in range (0,1) [55] is executed to intensify the brightness of laser speckle contrast (LSC). Fig. 7(B) is the LSC conversion. As a stimulation of actual pulses of human vision replication, the conversion of LSC to ROPE needs to be initiated. The conversion takes place from Equation (2) until Equation (5). Fig. 7 (C) visually depicts the conversion using ROP encoding [28], [62], [66], [68]. This concept previously used ROP as per stated in [52], [56], [57], [69].

Due to ESNN architecture being using as the backbone of this architecture, the sample sequence of spikes is encoded (spike trains) by using ROP scheme. Fig. 7(D), shows the conversion of the image into a newly formed image based neuron depth. The next step is to pre-process the image conversion of neural encoding into a convolution Equation (7a) using stochastic kernel and bias. This process generates the FM of the CL. By following a conventional flow of CNN architecture, the FM is fed into an activation function (ReLu) layer. ReLu function is to convert the negative value to zero and linear all passive value. Refer to Equation (8) and Equation (9a) for clarification and Fig. 7(E,F,G).

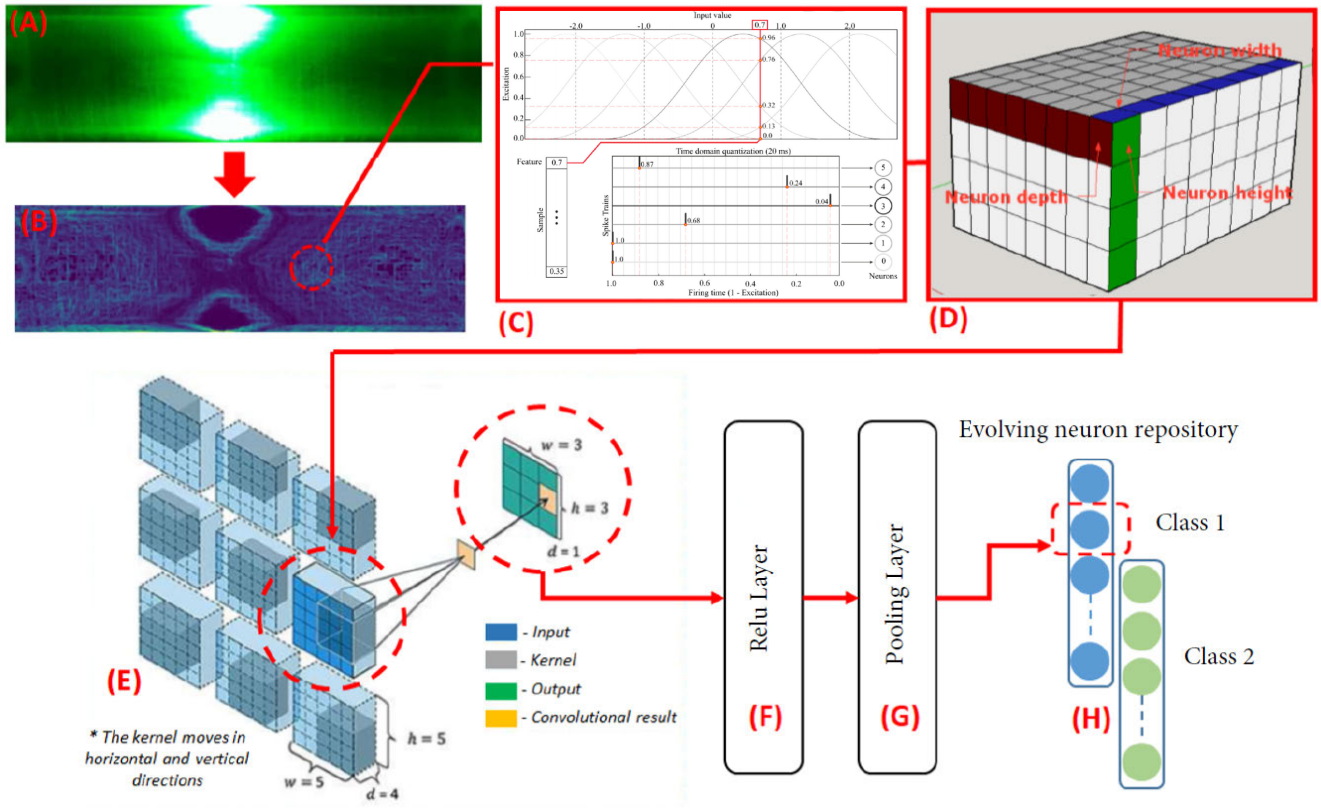

FIGURE 7. Proposed Deep learning Laser Speckle Contrast Evolving Spiking Neural Network (DL-LSC-ESNN) architecture.

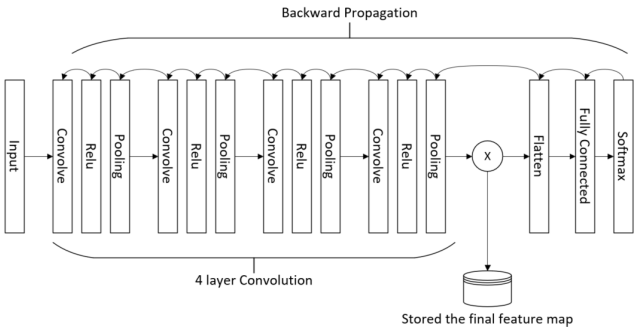

FIGURE 8. The technique to captured and stored final FM for visualization on the CNN approach.

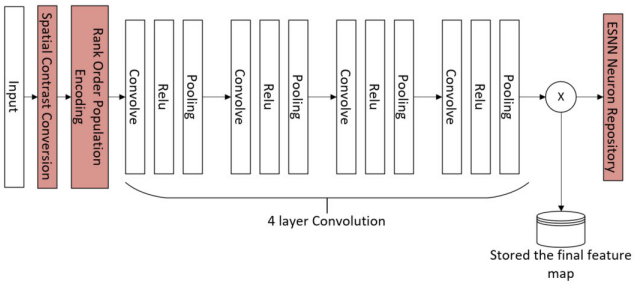

FIGURE 9. The technique to captured and stored final FM for visualization on the proposed DL-LSC-ESNN approach.

The PL's function is to reduce the size of feature map. As stated, the kernel will scan for max value within its kernel window. The kernel window is known as max pooling, as it is commonly used throughout the research community. Pooling important information will always reduce the size of each feature map by a factor of two.

After pre-processing, the essence of this neuron conversion is fed into an ESNN neuron repository learning algorithm. The learning algorithm eventually create output neuron, each with its own class label $I \in L$. The equations used in the training algorithm are Equation (11) until Equation (15). Fig. 7 (H) shows the high level evolving repository.

The algorithm composed of combination of LSC, CNN and ESNN. Fig. 10 is the DL-LSC-ESNN algorithm flow. Its start by initializing the neuron repository NR = {}, ESNN and CNN parameter (line 1 until 4). All the $images_s$ in $R\{images\}$ is converted from RGB to LSC domain (line 5 until 6). LSC aforementioned will use Equation (1). Equation (1) acted as ROI conversion of 5×5 windows for each $images_s$. The next step is to convert every pixel value in the into a neural encoding representative of the $SC\ Conversion_{\{a,b\}}$. This change $SC\ Conversion_{\{a,b\}}$ into a spike train domain (line 6 until 11), where $T_{p,q,r}$ is the simulation or spike interval. Fig. 7 (C) exemplifies the GRF encoding process for the feature of any given sample. The next step is to utilize conventional CNN flow (convolve, ReLu and pooling).

As mentioned above, CNNs are known to be good feature extractor. Their core utilization is to capture the essences of converted neural encoding $T_{p,q,r}$. A CNN algorithm

1. Initialized neuron repository NR = { }
2. Set eSNN parameter mod = [0, 1], C = [0, 1], SIM = [0, 1]
3. Set eSNN encoding parameter β, T, N
4. Set CNN kernel filter $K = \{3x3\}$, set $roih$ & $roiw = \{5,5\}$
5. For every $images_s$ in $\{image\}$ belonging to class c do
   $images_{s\{a,b\}}$, a is height, b is width
   $SC\ Conversion_{\{a,b\}} = \sum_{l=0}^{w-roiw}\sum_{m=0}^{h-roih} images_{s\{a+roih*m,b+roiw*l\}} * \frac{\sigma_{std\{roih*m,roiw*l\}}}{\langle I_{\{roih*m,roiw*l\}}\rangle}$
5. For every $pixel_j$ from $SC\ Conversion_{\{a,b\}}$ convert to GRF
7. $C_j = I^n_{min} + \frac{2j-3}{2}\left(\frac{I^n_{max}-I^n_{min}}{N-2}\right)$
8. $Wj = \frac{1}{\beta}\left(\frac{I^n_{max}-I^n_{min}}{N-2}\right)$
9. $output_j = exp\left(-\frac{(x-C_j)^2}{2W_j^2}\right)$
10. $T_{p,q,r} = |T(1-output_j)|$
11. end
12. For GRF convertion of $T_{p,q,r}$ do
13. $Convolve_{a,b,c} = \sum_{l=0}^{k-1}\sum_{m=0}^{w-1}\sum_{n=0}^{h-1} T_{sp+n,sq+m,r}K_{lmn} + B_{lmn}$
14. $ReLu_{a,b,c} = \begin{cases} 0 & for\ Convolve_{a,b,c} < 0 \\ Convolve_{a,b,c} & for\ Convolve_{a,b,c} \geq 0 \end{cases}$
15. $Pooling_{d,e,f} = \max_{a,b\in P_{i,j}} ReLu_{a,b,c}$, $P_{i,j}$ is the window for Pooling
16. $Pooling_{d,e,f}$ d represent array row, e represent array column and f is depth.
17. Perform transformation $Pooling_{d,e,f} \rightarrow Pooling_{d,ef}$
18. Create a new output neuron h and the connection weights as
19. $w_{g,h} = mod^{order(Pooling_{d,ef})}$
20. Calculate $PSP_{\max(h)} = \sum gw_{g,h} . mod^{order(Pooling_{d,ef})}$
21. Calculate PSP threshold value $\gamma_h = PSP_{\max(h)}.C$
22. If min distance (Newly output neuron weight vector,
23. Neuron repository weight vector in NR) ≤ SIM then
24. Update the weight vector and threshold of the most similar
25. neuron
26. $W_{g,h} = \frac{w_{new}+(w_{g,h}.M)}{M+1}$ And $\gamma_i = \frac{\gamma_{new}+(\gamma_i.M)}{M+1}$
27. else
28. Set M = M+1
29. Add the weight vector and threshold of the new output neuron to NR
    end
30. end

FIGURE 10. DL-LSC-ESNN Algorithm.

convolutes the row ( ) and column (q) followed by its neural encoding depth (r) with kernel acting as a pseudo filtration. This convolute is limited by boundaries within the converted neural encoding R[p,q,r]. The skipping factor (s) determine the resolution of convolution. Equation (7a) is the representation of a feedforward neural network by interpreting it is as a dot product between input tensor ($T_{p,q,r}$) and it kernel ($K_{l,m,n}$) by adding it with bias (B_{lmn}). Fig. 10 line 13 represent the equation. Fig. 10 line 13 until 15 is repetitive of the CL, Relu and PL. Its start with static kernel as first layer, followed by stochastic layer subsequently. The repetition of the layer depth is dependent on the input neuron conversion.

By capturing only the essences of its core neural encoding scheme, only the most important spike is contain. Next step is to utilize the ESNN training algorithm. For every pattern originating from the similar group, a new output neuron is generated and connected via weights $w_{g,h}$ to the previous layer of all pre-synaptic neurons. The value of $w_{g,h}$ is calculated through a synapse g based on the spike order as $w_{g,h} = mod^{order(Pooling_{d,e,f})}$, where g is the presynaptic neuron of the output neuron h (Fig. 10 line 19). Each neuron in this model can spike at most once, and when its PSP exceeds its threshold value, a neuron will be triggered. The PSP of a neuron i is defined as per Equation (12). A numerical threshold γ_h is set for the recently created output neuron as the fraction

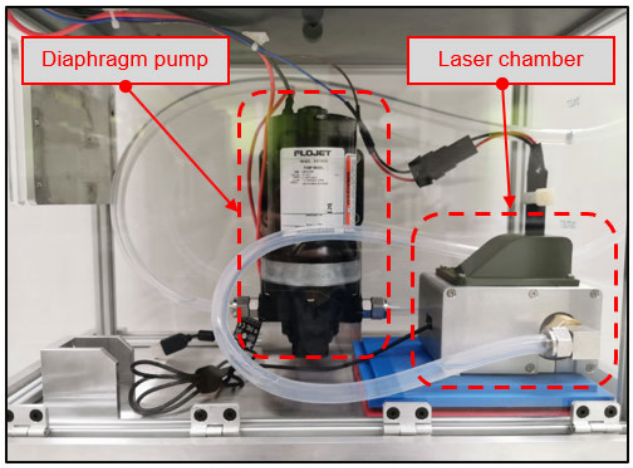

FIGURE 11. System hardware setup.

$C \in$ R (0, 1) of its maximum postsynaptic potential Fig. 10 (line 20) i.e. $\gamma_h = PSP_{max(h)}.C$ (line 21). A progressively generated output neuron's weight vector is then matched to the previously trained output neurons in the repository. When the Euclidean distance is smaller than the similarity parameter (SIM) between a newly generated output neuron weight vector and that of one or more of the already trained output neurons, they are regarded as similar. Consequently, their thresholds and vectors are accordingly combined. This can be observed from Fig. 10 in line 22 until 26, where M is the amount of prior neuronal combinations comparable to the ESNN's learning history. The latest created output neuron is discarded after assimilating and the latest model updates its weight vector. If similarity is not found (parameter logic of SIM) to recently created output neurons, it will be appended to its repository. The testing stage propagating spike via its trained output, which eventually encoded the test sample. Eventually, the class label of the test sample output neuron is fired first. It fires after a threshold value γ_h is activated.

VII. EXPERIMENTAL HARDWARE SETUP

Due to the HVM chiller's unpredictable nature, the experiment needed to further expand the detection method using a radical hardware approach. The discussion on the hardware setup is provided to clarify the technique of data collection and its main component. Fig. 11 is the high definition (HD) camera and laser chamber. The camera and laser chamber are designed to ensure the camera and laser are in a controlled environment. The chamber is designed using aluminum enclosure with black background as a control environment. On the lighting control, a monochromatic green laser (532nm) is chosen with a feedback control system via its switching regulator for a constant current and voltage supply. All the setup is obligated to ensure no external lighting will distort the internal chamber environment. Fig. 11 also shows the diaphragm pump, the functionality of the pump is to distort the targeted HFE chemical by using forceful kinetic motion of the diaphragm blade.

The system key element of detection is the observation windows. The observation windows used a polycarbonate material. The material is chosen to ensure that it was able to withstand extreme pressure and temperature. The system monitored chiller behavior via its internal tank circulatory, and the tank acted as a central collective for HFE chemical that is connected to heat exchanger and closely simulated the after effect condition. The after effect condition is when the evaporator and condenser are being process and thru its pseudo contact via heat exchanger eventually will provide the highest chemical combination. As the objective of the system is to detect the contamination of HFE inside the chiller tank, this method of testing uses ambient temperature; this is important for a safety perspective.

VIII. RESULTS AND DISCUSSION

A. DATASET VISUALIZATION AND SIMILARITY MEASUREMENT

The visualization of impurities HFE dataset eventually provide an understanding of the level of difficulties of how the dataset structures are associated with each other. To perform this task, the visualization mechanism of t-distributed stochastic neighbor embedding (t-SNE) is applied. Historically, t-SNE [70] has been efficient when it comes to finding the underlying data structure. The main idea behind t-SNE is to preserve the local data structure through the preservation of pairs of data from the original space to the future space [71]. As previously discussed, the stochastic behavior of the impurities HFE detection relies on that to visualize the nature of the image data distribution. This visualization provides extensive understanding on the interaction of each sample of the data structure. The t-SNE with its ability to persevere and finding underlying data structure is the most suitable visualization technique for stochastic based dataset. On the other hand, t-SNE is particularly designed to avoid this dense clustering of impurities in HFE detection, which makes it possible to visualize large, high dimensional data systems in a clearer way [70]. Due to the research nature and inspired by the parametric t-SNE [72], the usage of tSNE is presented with an explicit nonlinear function in this research. The visualization of the raw image dataset is shown in Fig. 12.

The qualitative visualization of Fig. 12 shows that the data are non-separable or non-linear (PHFE indicated - Pure HFE and xPHFE indicated contaminated HFE). For a sample of impurities HFE dataset, there are no clear boundaries between subtypes of sample. They are highly comingled and certain data points see complete assimilation. This gives a clear picture of the difficulties to classify the HFE contamination and thus required LSC domain conversion and RN cubic form creation to increase the dimensional additive.

To further support the qualitative argument of original visual dataset assimilation. Fig. 13 (A) and (B) are the representation of cosine similarity between Pure and contaminate HFE. The visualization of the dataset utilized cosine similarity to measure the similarity of each images. As cosine similarity works really well on comparing each dataset

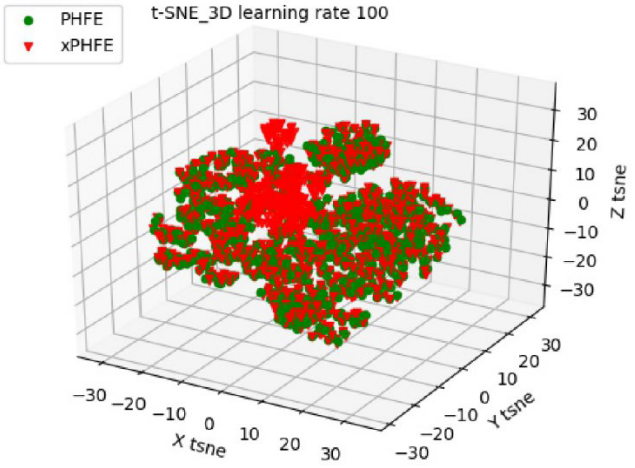

FIGURE 12. Visualization of Impurities HFE dataset.

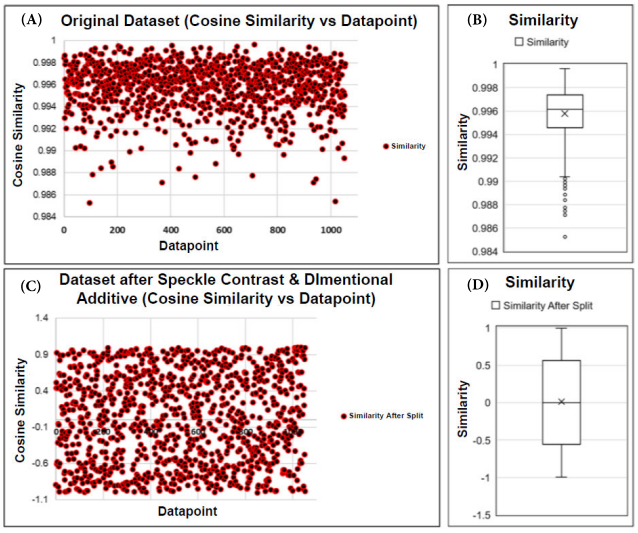

FIGURE 13. Dataset similarity result pre and post processing.

irrespective of their size, the technique works by measuring the cosine angle between two vectors projected in multidimensional space [73]–[79]. As for the highest similarity value is referring to 1. From Fig. 13 (A), referring to original dataset the spread is mostly accumulated at 1. Which indicated that similarity strongly occurs. From Fig. 13 (B), the mean of similarity is at 0.996, spreading is between 0.997 and 0.995. This indicated how narrow and accumulated the similarity between pure and contaminate HFE dataset.

B. BASELINE SETUP AND RESULTS

A proper accuracy validation between state of the art (known DL architecture) is needed against DL-LSC-ESNN architecture. This to ensure that DL-LSC-ESNN is highly competitive against well-known DL architecture. Here the study are comparing DL-LSC-ESNN against state-of-the-art architecture such as ResNet [80]–[82], VGGNet [83]–[85] and Inception Net [86]–[88]. Refer to Table 2 for state-of-the-art accuracy.

TABLE 1. Baseline rudimentary CNN architecture.

CNN Architecture	Accuracy (%)
CNN 3 layer (8 FM 3x3 kernel)	62.87
CNN 3 layer (8 FM 5x5 kernel)	58.23
CNN 3 layer (16 FM 3x3 kernel)	61.52
CNN 3 layer (16 FM 5x5 kernel)	55.51
CNN 3 layer (32 FM 3x3 kernel)	62.66
CNN 3 layer (32 FM 5x5 kernel)	58.11
CNN 4 layer (8 FM 3x3 kernel)	63.64
CNN 4 layer (8 FM 5x5 kernel)	59.34
CNN 4 layer (16 FM 3x3 kernel)	63.23
CNN 4 layer (16 FM 5x5 kernel)	59.20
CNN 4 layer (32 FM 3x3 kernel)	62.23
CNN 4 layer (32 FM 5x5 kernel)	59.20

DL-LSC-ESNN was built upon a layer of rudimentary CNN. As aforementioned the CNN layers acted as FE for DL-LSC-ESNN. Due to the usability and functionality a characterization baseline is highly needed to further strengthen the validation accuracy via a rudimentary CNN baseline case study. For a rudimentary CNN experimentation the filter weights of each layer are initialized by randomly generated from Gaussian distribution (mean value $\mu = 0$ and standard deviation $\sigma = 0.001$), bias is set to stochastic. The kernel size is 3×3 or 5×5. As for convolution layer properties such as pooling and activation layer, for this research pooling will be maximum function and for the activation layer, ReLu will be selected. The learning rate selected is at 0.0001 [13], [89], [90], epoch is 500 [90] and momentum rate is 0.0001 [91]. Refer to Table 1 for rudimentary CNN accuracy.

The baseline rudimentary CNN accuracy (refer to Fig. 26) being generated to further investigated the optimized layer for the highest accuracy for HFE dataset. By adding or lowering the layer, the accuracy offset gave a quartile of ∼62.66 and ∼58.11 with its maximum accuracy is at 63.64. The spreading indicated the diversity of the layer impacting accuracy. Thus indicated by adding more layer the accuracy will be further decreasing. For this experimentation, the CNN setup is a 4 layer with 3×3 and 5×5 kernel as a rudimentary baseline for CNN case study.

C. DL-LSC-ESNN CHARACTERIZATION AND RESULT

From the perspective of architecture differences by referring to Fig. 4 and Fig. 7, DL-LSC-ESNN adds layers to the LSC domain by utilizing Equation (1). The initial transformations of the domain from conventional CNN's RGB (refer to Fig. 4) as its inputs to the LSC domain are achieved through Equation (1). DL-LSC-ESNN also added a dimensional additive layer of RN after LSC domain (refer to Fig. 7 C and D). Fig. 7 C, utilizing Equation (2) until Equation (5). Equation (2) and Equation (3) is the definitive parameter that necessitates being set as initial calculation (C_j and W_j). The purpose of Equation (4) and Equation (5) is to generate a spike train from a numeric conversion. The intention is to build a cubic representative of LSC domain by referring to Fig. 7 D. Fig. 7 D is the finalization of dimensional additive that needs to be added before feeding the RN cubic form into iterative layers

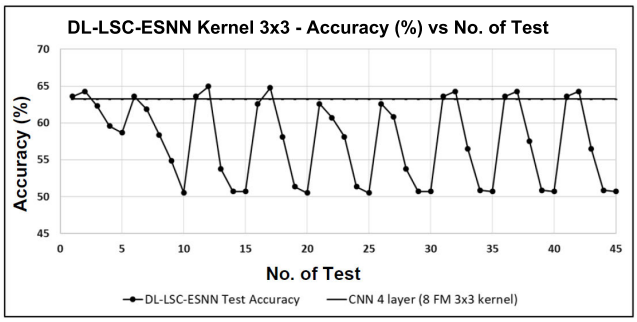

FIGURE 14. DL-LSC-ESNN Result vs CNN with 3 × 3 kernel filter.

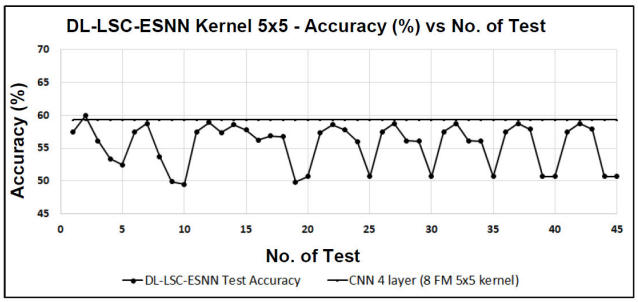

FIGURE 15. DL-LSC-ESNN Result vs CNN with 5 × 5 kernel filter.

of CL, Relu and PL. After the iterative layers, the final FM is generated. The final FM which represents the essences of spike train is fed in an evolving repository (refer to Fig. 7 H). The distinctive difference by comparing to CNN is that DL-LSC-ESNN adds layers of LSC domain conversion, RN cubic form creation, and ESNN neuron repository. The enhanced architecture of DL-LSC-ESNN eventually strengthen the classification of HFE impurities detection by improving its accuracy.

As per Fig. 14 result show the highest accuracy at 64.94% with similarity (SIM) 0.3 and threshold (TH) 0.6. The characterization of parameter SIM is defined by Fig. 19 is within SIM $\mathbb{R}\{0.1, 0.9\}$ and TH is within $\mathbb{R}\{0.5, 0.9\}$, with incremental resolution of 0.1 respectively. By comparing to baseline CNN experimentation results. The $\triangle$ *accuracy* is at ∼ 1.3%. This interesting result advocate for one of our postulated hypothesis. The dimension additive after SC conversion with GRF able to provide even more noticeable separation and differentiation of pure and contaminated HFE as per depicted by Fig. 17. The quantifiedFig. 17 can be viewed in terms of Fig. 13 (C and D), from the figure the similarity is spreading rather than accumulated at 1 (the highest similarity). Fig. 13 (D) shows that the spreading is widen by quantile of 0.5 and -0.5 compared with Fig. 13 (B) quantile which is at 0.997 and 0.995 respectively. The spreading of Fig. 13 (D) thus support the aforementioned postulated hypothesis that dimensional additive able to separate the pure and contaminated HFE effectively. The similarity result of the DL-LSC-ESNN's FE layer is referring to Fig. 17 which is the capturing result at Fig. 7 (G) after PL. The result is

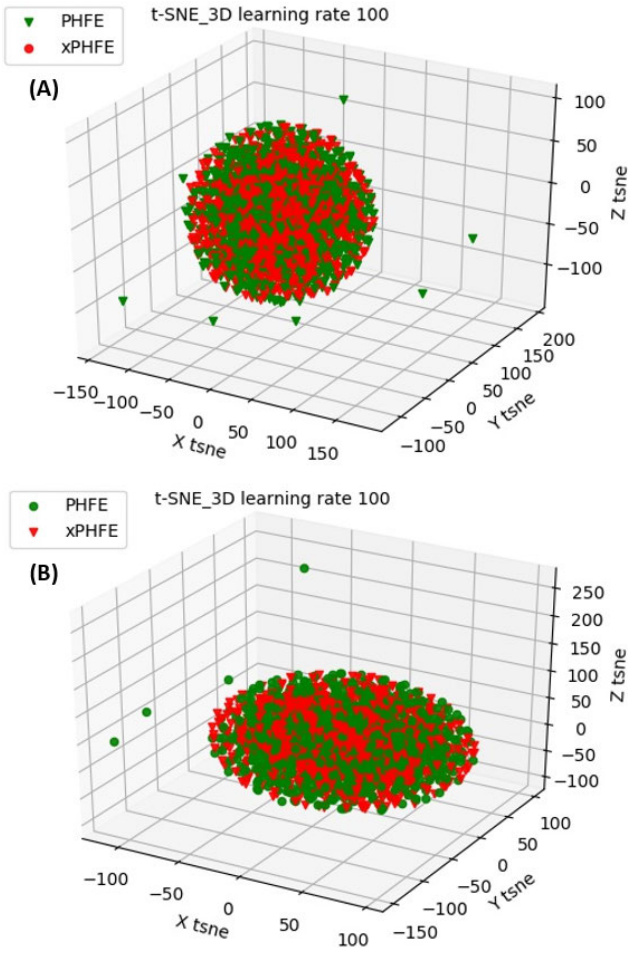

FIGURE 16. tSNE visualization of CNN result of 4 layer 3 × 3 and 5 × 5 kernel filter. (A) is 3 × 3 4l CNN and (B) is 5 × 5 4l CNN.

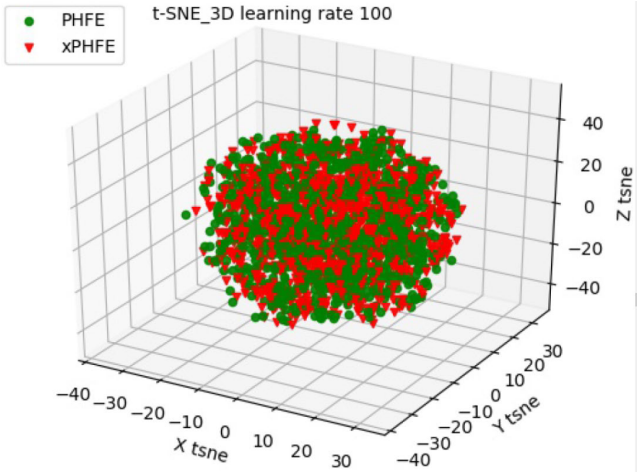

FIGURE 17. tSNE visualization of DLESNN result of 4 layer 3 × 3 kernel filter with neuron of 10.

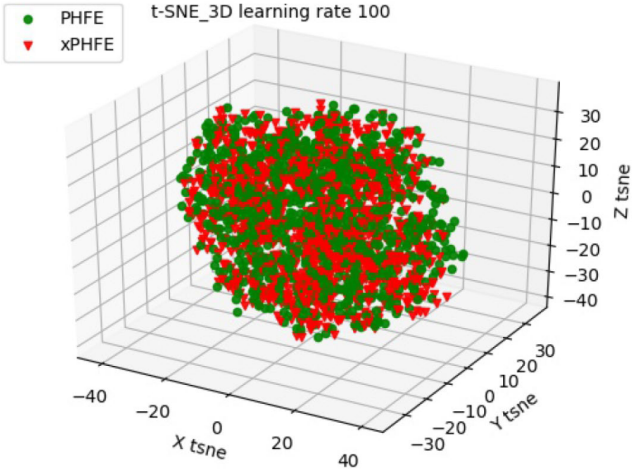

FIGURE 18. tSNE visualization of DLESNN result of 4 layer 5 × 5 kernel filter with neuron of 10.

stored and view for better understanding on the after effect of several iterations of FE layers. Fig. 16 (A) is the CNN using 3 × 3 with 4 layer of convolution. The final FM is captured and stored after several convolution layer repetitions (refer to Fig. 8). The active capturing technique is to get a proper visualization of 4 layer CNN FM conditions and clarifying the initial result of baseline kernel 3 × 3 CNN accuracy of 63.64%. The experimentation shows the conglomeration of pure HFE and contaminate HFE for kernel 3 × 3. The active capturing and storing method shows that there is no distinctive separation or non-linear disconnection between Pure and Non-Pure HFE (refer to Fig. 16 (A)). As stated in this conglomeration visualization, the accuracy is 63.64% for baseline CNN. The technique of visualization on the final FM's DL-LSC-ESNN is shown in Fig. 9. For this research, after 4 layer convolutions, the FM is stored and observed. This is to get a precise outcome of how the data FM's final tensor structure of baseline CNN (refer to Fig. 8) against the proposed method DL-LSC-ESNN (refer to Fig. 9) is distinguished.

Fig. 15 and Fig. 20 are the results of 4 layer convolutions of DL-LSC-ESNN with 5 × 5 kernel filters. The highest $\triangle$ *accuracy* compared with CNN baseline is at 0.58%. Again this aligns with the initial analysis that dimension additive eventually improved the accuracy of detection. Fig. 18 contains the results of the aftereffect of the FE layer and shows the effect of dimension additive decomposing and splitting between Pure and Non-Pure HFE; note the separation of differentiation through its expansion. Fig. 16 (B) is the 4 layer 5 × 5 CNN, the visualization of the conglomeration between pure HFE and Non-Pure HFE is undeniable. The correlation between initial experimentation of DL-LSC-ESNN 3 × 3 and 5 × 5 kernel filter highest $\triangle$ *accuracy* is at 5.02%. Nevertheless, the $\triangle$ *accuracy* is differentiated by minor changes, demonstrating that the selection of kernel filter size does affect the accuracy. Fig. 18 is the 4 layer 5 × 5 kernel filters, aforementioned regarding the method of capturing and storing the final FM. In Fig. 18 the visualization of the decomposing of final FM data between Pure and Non-Pure HFE is properly visualized.

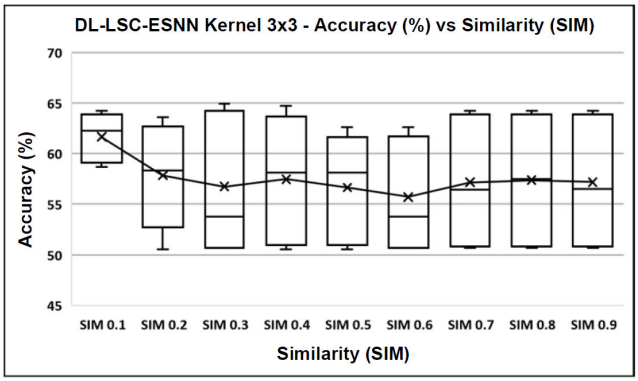

FIGURE 19. Kernel 3 × 3 Accuracy (%) vs Similarity (SIM) parameter characterization of 10 neuron.

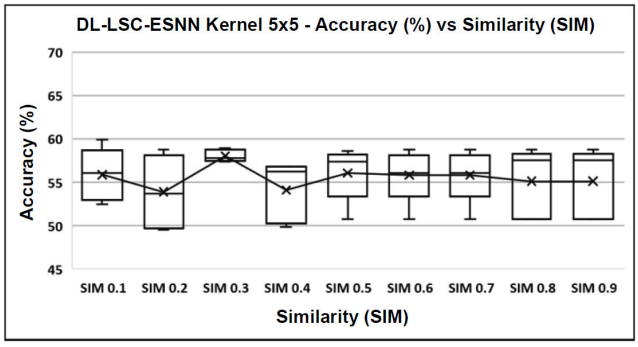

FIGURE 20. Kernel 5 × 5 Accuracy (%) vs Similarity (SIM) parameter characterization of 10 neuron.

Fig. 19 and Fig. 20 provide visibility of observing the stability of kernel 3 × 3 and 5 × 5. Fig. 19 for SIM 0.3,0.7,0.8 and 0.9 displays a steady variation of accuracy. The steady variation indicated that the variation is not limited to inadequate $\triangle accuracy$ of change. The steady variation of SIM, therefore, contribute a more eminent indication that during this episode of mentioned SIM, the assimilation of ESNN repository weighting via Equation (14) is profoundly evolving and thus able to get a vaster variation of accuracy. SIM 0.3 yielded the highest accuracy with a steady variation. SIM 0.5 and 0.6 were imperceptibly less than the aforementioned SIM parameter but with a vaster variation of accuracy. SIM 0.1 shows diminutive and limited variations. Fig. 21 depicted the relationship between Accuracy (%) versus the Threshold (TH) parameter. From the experimentation analysis, TH 0.6 yielded the highest accuracy with the normalized distribution. If correlated with TH 0.5 and 0.9, the accuracy is lower, and the distribution is tight. This indicated a minimum variation of TH 0.5 and 0.9, even though TH 0.7 and 0.8 indicated high variation. Similarly, the accuracy is lower than TH 0.6. Therefore, the summarization for kernel 3 × 3 with its initial parametric of SIM 0.3 and TH 0.6. From the results of the experiment in Fig. 21, based on its highest accuracy, the parameter mentioned is the most suitable to further expanded the experimentation.

Toward Fig. 20 of 5 × 5 kernel, the variation of accuracy is less than Fig. 19 3 × 3 kernel by the aforementioned

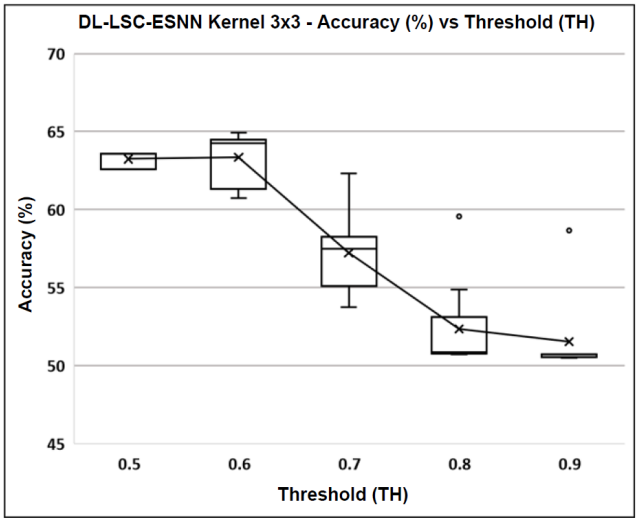

FIGURE 21. Kernel 3 × 3 Accuracy (%) vs Threshold (TH) parameter characterization of 10 neuron.

maximum $\triangle accuracy$ 5.02%. Further investigation from Fig. 20 of parameter SIM 0.2,0.8 and 0.9 indicated similarity of accuracy variation between the experimental parameters. Fig. 20 of SIM 0.5,0.6 and 0.7 as observed display similarity of accuracy variation. By comparing the accuracy variation between kernel 3 × 3 versus 5 × 5, kernel 5 × 5 shows a more moderate accuracy variation as per kernel 3 × 3. Thus, the evolving assimilation using Equation (14) is obtained. Kernel 5 × 5 moderate variation is shown by its FM, which is lower than kernel 3 × 3. The important aspect is that a lower variation of final FM parameter also indicated minor complexity of calculation. With less FM, the computation is shorter, and thus its computation is quicker than kernel 3×3. The analysis further observed the performance of kernel 5 × 5 by referring to Fig. 22. TH 0.5 and 0.6 show restricted variation. The analysis indicated that the TH parameter does have an impact on the accuracy of detection. SIM 0.7 and 0.9 display an accuracy variation difference. Fig. 22 of TH 0.8 indicates accuracy variation spreading, thus attesting to wider optimization. Unfortunately, in the perspective of accuracy SIM 0.5,0.7,0.8 and 0.9 is lower than SIM 0.6. Therefore, the experimentation referring to Fig. 22 for kernel 5 × 5 presents a parametric value of SIM 0.1 and TH 0.6 to further extended the experimentation.

Proceeding to Fig. 24 (A) and (B), the experimentation renders clarity upon Accuracy (kernel 3 × 3) on SIM 0.3 and TH 0.6 versus Receptive Neuron (RN). The aforementioned parameter is selected as previous experimentation the accuracy is at the highest for RN 10. Through experimentation of characterization sweep referring to Fig. 24(A), by observing it closely, the accuracy displays a non-linear movement of every RN. However, the experiment from Fig. 24 (A) reveals a better understanding of the kernel 3×3 accuracy (%) versus RN. Due to the detailed performance of the characterization sweep of every RN parameter. It further increases the understanding of the RN's significant accuracy differences. From

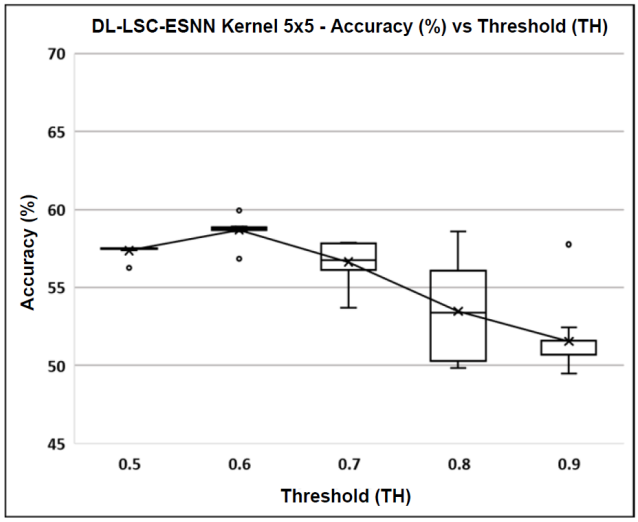

FIGURE 22. Kernel 5 × 5 Accuracy (%) vs Threshold (TH) parameter characterization of 10 neuron.

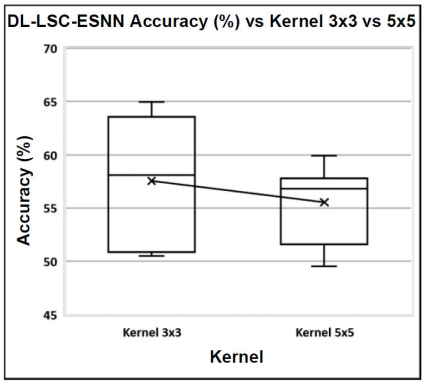

FIGURE 23. Accuracy (%) vs Kernel 3 × 3 and 5 × 5 characterization of 10 neuron.

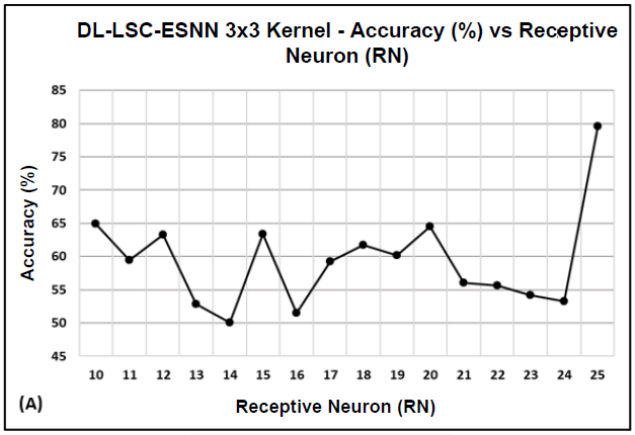

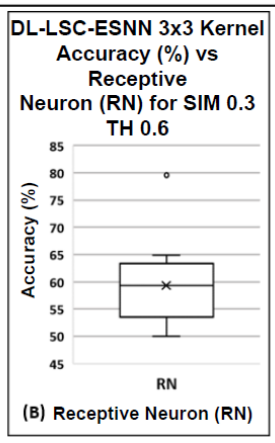

FIGURE 24. Characterization of kernel 3 × 3 for SIM 0.3 and TH 0.6 accuracy (%) vs Receptive Neuron $\mathbb{R} \in (10, 25)$.

Fig. 24 (A) analysis, RN 25 accuracy is at 79.57%, RN 16 is the lowest at 50.08, which is lower than the baseline CNN (63.64%). Analysis of Fig. 24 (A) of RN 25 produced the highest accuracy, to clarify this refer to Fig. 7 (C) on the encoding scheme. During this condition on the population encoding, the pulses' conversions took place. RN 25 provides the most accurate representation of the numeric value. The SC spike conversion is correctly represented as a completed stimulation of spikes. This is due to the previously mentioned fact that single spikes can, in principle, carry substantial information about visual stimuli [50]. This is the indication that during RN 25 with parameter TH is at 0.6 and SIM is 0.3. The highest characterization during kernel 3×3 accuracy now at 79.57%.

The experimentation extends further by completing the characterization sweep on kernel 5 × 5 for Accuracy (%) vs RN (refer to Fig. 25) the parameter is being referred to previous experimentation SIM 0.1 and TH 0.6 value. This parameter was selected as it produced the highest accuracy during the initial experimentation of TH and SIM parameter characterization sweep for 5 × 5 kernel (Fig. 20 and Fig. 22).

As kernel 5 × 5 had lower accuracy compared to kernel 3 × 3 during the initial experimentation, kernel 5 × 5 thus renders a more simplistic and moderate FM parameter refinement. After running several RN characterization sweep $\mathbb{R}\{11, 25\}$. From Figure 20, the RN 15 yielded the highest accuracy at 80.51%. As per analysis throughout this condition on the population encoding, as for the pulses' conversion took place the RN 15 learning is substantial enough to represent both spiking rate and time spatiotemporal structural information within a ventral stream, refer to Fig. 7 (C) on the encoding scheme. The result produced by RN 23 is the second-highest accuracy at 75.535% followed by RN 16 which accuracy at 69.38%. Further investigation on RN 11-14, 17-22 and 24-25 indicated that during its conversion from SC domain toward GRF it does, however, contain a spike train overlap, and the information if translated accordingly is interpreted as in compression or concentrated state. Where the specific condition of the spike train is accumulated at a single point during GRF conversion. By referring to Fig. 7(C), it does, however, explicates during GRF conversion the spike compression. Aforementioned by the receptive fields which allow continuous values to be encoded using a set of neurons with overlapping sensitivity profiles. Each input variable is represented independently by one-dimensional receptive field unit M. For variable n of the interval $[I_{min}, I_{max}]$ is defined. The

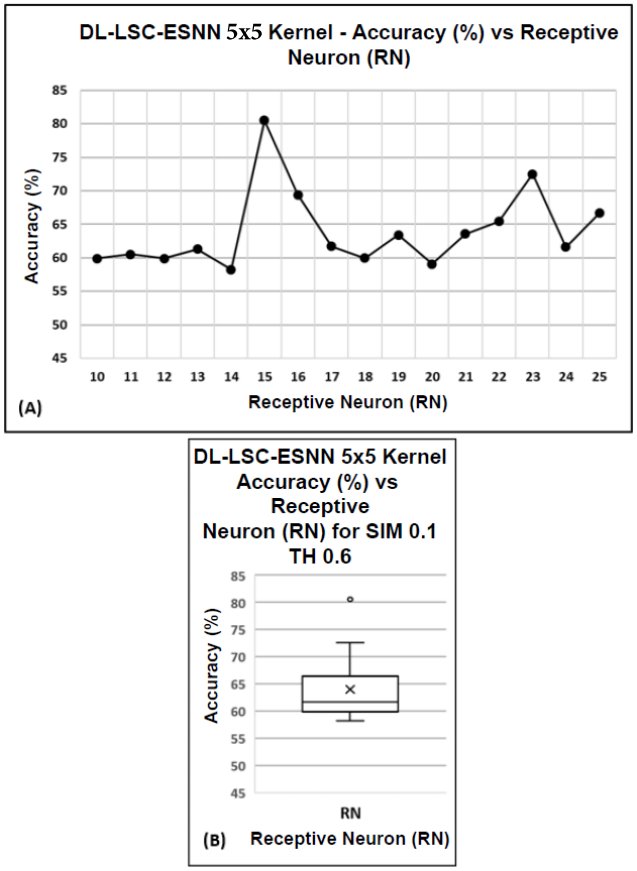

FIGURE 25. Characterization of kernel 5 × 5 for SIM 0.1 and TH 0.6 accuracy (%) vs Receptive Neuron $\mathbb{R} \in (10, 25)$.

Gaussian receptive field of neuron j is given by its center. As shown in Fig. 7(C), the Gaussian receptive interception is indicated as higher. There's a state of information compression that impacted the information representation. Lastly, Fig. 25 (B) shows the variation of RN, this indicated the variation of the distribution of its accuracy. No compression or limitation for further optimization exits.

Ultimately, two states of high accuracy are achieved: for kernel 3 × 3 the selected parameter is SIM 0.3 and TH 0.6. This parameter's final result shows an accuracy of 79.57%. From the analysis of kernel 3 × 3, the kernel is small and able to produce a significant accuracy of variation for expanding optimization as mentioned and shown in Fig. 24 (A and B). But a small kernel indicates extended time to train as compared with kernel 5 × 5. Moreover, kernel 3 × 3 does not show multiple excitations of accuracy fluctuation for its RN characterization sweep as shown in Fig. 24A. Kernel 5×5 eventually, yielded the highest accuracy at 80.51%. Even though the kernel is higher and wider, and initial experimentation analysis indicated narrow active optimization. Kernel 5 × 5 is considered suitable and exits in much more direct optimization (refer to Fig. 22 and Fig. 23). Furthermore, kernel 5 × 5 does present a distinctive ability to shrink its parametric FM. Fig. 25 (A and B), indicated improvement of Accuracy(%) by expanding the experimentation through

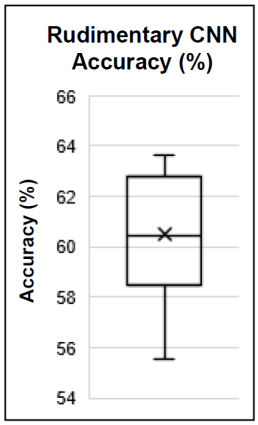

FIGURE 26. Rudimentary CNN result.

TABLE 2. Baseline DL state-of-the-art architecture accuracy.

State of the art architecture	Accuracy (%)
RESNet	76.81
VGGNet	50.47
InceptionNet	57.54

RN variation. From Fig. 25A, the excitation fluctuations of Accuracy (%) for RN 15, 16 and 23 are shown. This indicates that for kernel 5 × 5, its ability to access certain accuracy excitation is considered an advantage. Conclusively, the add-on advantages acted as a countermeasure to initial narrow optimization (refer to Fig. 22 and Fig. 23) for kernel 5 × 5 is by characterization sweeping of the RN within the distinctive range. By doing this step. It shows a significant improvement in its accuracy (%) of variation, refer to Fig. 25B. This indicated the optimization is expanding and thus increased its probable state of getting high accuracy. The RN variation for kernel 5 × 5 aforementioned indicated accuracy higher than kernel 3 × 3. Thus, the finalization of the DL-LSC-ESNN parameter is concluded as SIM 0.1, TH 0.6 and RN 15 at kernel 5 × 5.

The finalization of DL-LSC-ESNN characterization gave final accuracy and its configuration, nevertheless by comparing it to RESNet (refer to Table 2), the △ *accuracy* now is at 3.7%. RESNet able to give the highest accuracy due to its ''identity shortcut connections''. ResNet stacks up identity mappings, layers that initially do not do anything, and skips over them, reusing the activation from previous layers. This compression ability add extra boost of performance compared with other state-of-the-art architecture (ResNet vs VggNet △ *accuracy* is at 26.34% and ResNet vs InceptionNet △ *accuracy* is at 19.27%). Further investigation also shows that by comparing RESNet with rudimentary CNN the △ *accuracy* is at 13.17%. Even though ResNet gave the highest accuracy, it is hard to train because of the notorious vanishing gradient problem. This is due to the gradient is back-propagated to earlier layers, repeated multiplication may make the gradient infinitive small. As a result, as the network goes deeper, its performance gets saturated or even

starts degrading rapidly. This behaviors also being observed for InceptionNet and VGGNet.

IX. CONCLUSION AND FUTURE WORKS

The DL-LSC-ESNN eventually overcome conventional CNN for HVM HFE impurities LSC polycarbonate application. This is achievable through the added layers of LSC domain conversion, RN cubic form creation and ESNN neuron repository evolving ability to generate and assimilation of new weight. To put it into perspective DL-LSC-ESNN architecture are purely a feedforward algorithm, while conventional CNN using a combination of feedforward and backpropagation algorithm. The proposed technique of LSC domain conversion is highly practical in HFE impurities detection by significantly improving the $\triangle$ *accuracy* of detection by 3.7% comparing to state-of-the-art CNN architecture. The significance of a 3.7% improvement referred to HVM chiller usability for industrial application. Each chiller integrated into the handler that indirectly involved a CPU cyclic thermal validation. Each hour the handler's CPU output is in a hundred thousand units. This reflected upon the detectability accuracy which is at 3.7% improvement. Under HVM is deemed highly impactful due to the output vs accuracy improvement**.** The DL-LSC-ESNN is also able to get higher accuracy by using a rudimentary CNN architecture without dependencies in an increasing layer of CNN. Thus, in term of numbers parameter to be trained it is considered in a compressed mode. The research also manages to dictate the separation of the dataset which eventually assisting in classifying between pure and Non-pure HFE. The dimensional additive methodology thus provides a robust process by added a new technique of quantified SC attributes creation on polycarbonate LSC encoding by seamlessly integrating with GRF encoding. Ultimately, the proposed enhanced architecture is able to provide significant improvements for throughput usability throughout the industry usage model by drastically increased its detection rate. As mentioned, by adding several features by looking at different perspective the enhanced technique of integration and assimilation of multiple attributes eventually contributed to this significant improvement.

As for accuracy augmentation for LSC HFE impurities detection, several suggestions to the enhancement of accuracy need to be considered for future implementation and improvement. The exploration of applying probabilistic evolving spiking neural network (PESNN) architecture is the next inline implementation. The PESNN applies quantum probabilistic properties to ESNN weight. The approach is to create a probabilistic state of each neuron weight connection that eventually assist in providing a higher ability to assimilate or generated new neuron repository. The new additive process methodology should be able to augment accuracy detection even further.

REFERENCES

[1] Z. K. Nagy, A. E. Hagrasy, and J. Litster, *Continuous Pharmaceutical Processing*. New York, NY, USA: Springer, 2020.
[2] D.-H. Lee, J.-K. Yang, C.-H. Lee, and K.-J. Kim, "A data-driven approach to selection of critical process steps in the semiconductor manufacturing process considering missing and imbalanced data," *J. Manuf. Syst.*, vol. 52, pp. 146–156, Jul. 2019.
[3] M. Hassoun, D. Kopp, L. Mönch, and A. Kalir, "A new high-volume/low-mix simulation testbed for semiconductor manufacturing," in *Proc. Winter Simulation Conf. (WSC)*, 2019, pp. 2419–2428.
[4] X. Xia, W. Liu, Z. Zhang, L. Wang, J. Cao, and X. Liu, "A balancing method of mixed-model disassembly line in random working environment," *Sustainability*, vol. 11, no. 8, p. 2304, Apr. 2019.
[5] S. Kumar, V. Manjrekar, V. Singh, and B. Kumar Lad, "Integrated yet distributed operations planning approach: A next generation manufacturing planning system," *J. Manuf. Syst.*, vol. 54, pp. 103–122, Jan. 2020, doi: 10.1016/j.jmsy.2019.12.001.
[6] M. B. Frs and H. S. Green, "A kinetic theory of liquids," *Nature*, vol. 159, no. 4034, p. 251, 1947.
[7] C. Cercignani, "The Boltzmann equation," in *The Boltzmann Equation and its Applications*. New York, NY, USA: Springer, 1988, pp. 40–103.
[8] C. Cercignani and M. Lampis, "On the kinetic theory of a dense gas of rough spheres," *J. Stat. Phys.*, vol. 53, nos. 3–4, pp. 655–672, Nov. 1988.
[9] S. Pan and T. S. Storvick, "Kinetic theory calculations of pressure effects of diffusion," *J. Chem. Phys.*, vol. 97, no. 4, pp. 2671–2681, Aug. 1992.
[10] R. Kapral, "Kinetic theory of chemical reactions in dense fluids," *J. Chem. Phys.*, vol. 68, no. 4, pp. 1903–1912, Feb. 1978.
[11] H. C. Lai, T. F. Chew, and N. A. Razak, "Evaluation of particle image velocimetry measurement using multi-wavelength illumination," *IOP Conf. Mater. Sci. Eng.*, vol. 370, p. 12044, Nov. 2018.
[12] B. Chu, *Laser Light Scattering: Basic Principles and Practice*. Chelmsford, MA, USA: Courier Corporation, 2007.
[13] S. Cai, S. Zhou, C. Xu, and Q. Gao, "Dense motion estimation of particle images via a convolutional neural network," *Experim. Fluids*, vol. 60, no. 4, p. 73, Apr. 2019, doi: 10.1007/s00348-019-2717-2.
[14] Y. Lee, H. Yang, and Z. Yin, "PIV-DCNN: Cascaded deep convolutional neural networks for particle image velocimetry," *Experim. Fluids*, vol. 58, no. 12, p. 171, Dec. 2017.
[15] X. Qu, Y. Song, Y. Jin, Z. Guo, Z. Li, and A. He, "3D particle field reconstruction method based on convolutional neural network for SAPIV," *Opt. Exp.*, vol. 27, no. 8, pp. 11413–11434, 2019.
[16] T. G. Mason, H. Gang, and D. A. Weitz, "Rheology of complex fluids measured by dynamic light scattering," *J. Mol. Struct.*, vol. 383, nos. 1–3, pp. 81–90, 1996, doi: 10.1016/s0022-2860(96)09272-1.
[17] R. Pecora, "Dynamic light scattering measurement of nanometer particles in liquids," *J. nanoparticle Res.*, vol. 2, no. 2, pp. 123–131, 2000.
[18] D. Chicea and S. M. Rei, "A fast artificial neural network approach for dynamic light scattering time series processing," *Meas. Sci. Technol.*, vol. 29, no. 10, Oct. 2018, Art. no. 105201, doi: 10.1088/1361-6501/aad937.
[19] A. Turpin, I. Vishniakou, and J. D. Seelig, "Light scattering control in transmission and reflection with neural networks," *Opt. Exp.*, vol. 26, no. 23, p. 30911, 2018, doi: 10.1364/oe.26.030911.
[20] A. Yevick, M. Hannel, and D. G. Grier, "Machine-learning approach to holographic particle characterization," *Opt. Exp.*, vol. 22, no. 22, p. 26884, 2014, doi: 10.1364/oe.22.026884.
[21] P. Saini, C. M. Arndt, and A. M. Steinberg, "Development and evaluation of gappy-POD as a data reconstruction technique for noisy PIV measurements in gas turbine combustors," *Experim. Fluids*, vol. 57, no. 7, p. 122, Jul. 2016, doi: 10.1007/s00348-016-2208-7.
[22] E. Fleischhauer, F. Azimi, P. Tkacik, R. Keanini, and B. Mullany, "Application of particle image velocimetry (PIV) to vibrational finishing," *J. Mater. Process. Technol.*, vol. 229, pp. 322–328, Mar. 2016, doi: 10.1016/j.jmatprotec.2015.09.017.
[23] C. Pan, D. Xue, Y. Xu, J. Wang, and R. Wei, "Evaluating the accuracy performance of Lucas-Kanade algorithm in the circumstance of PIV application," *Sci. China Phys., Mech. Astron.*, vol. 58, no. 10, Oct. 2015, Art. no. 104704, doi: 10.1007/s11433-015-5719-y.
[24] I. D. Block and F. Scheffold, "Modulated 3D cross-correlation light scattering: Improving turbid sample characterization," *Rev. Sci. Instrum.*, vol. 81, no. 12, Dec. 2010, Art. no. 123107.
[25] I. Goodfellow, Y. Bengio, and A. Courville, *Deep Learning*. Cambridge, MA, USA: MIT Press, 2016.
[26] W. Gerstner and W. M. Kistler, *Spiking Neuron Models: Single Neurons, Populations, Plasticity*. Cambridge, U.K.: Cambridge Univ. Press, 2002.
[27] N. Kasabov, K. Dhoble, N. Nuntalid, and A. Mohemmed, "Evolving probabilistic spiking neural networks for spatio-temporal pattern recognition: A preliminary study on moving object recognition," in *Proc. Int. Conf. Neural Inf. Process.* Cham, Switzerland: Springer, 2011, pp. 230–239.

[28] S. Schliebs and N. Kasabov, "Evolving spiking neural network—A survey," *Evolving Syst.*, vol. 4, no. 2, pp. 87–98, Jun. 2013.
[29] A. S. Arya, V. Ravi, V. Tejasviram, N. Sengupta, and N. Kasabov, "Cyber fraud detection using evolving spiking neural network," in *Proc. 11th Int. Conf. Ind. Inf. Syst. (ICIIS)*, Dec. 2016, pp. 263–268.
[30] B. G. Zagar and J. Lettner, "A discussion of sources of error in laser-speckle based systems," *Int. Soc. Opt. Photon.*, vol. 8306, Oct. 2011, Art. no. 830606.
[31] G. R. C. Reddy and V. V. Rao, "Correlation of speckle patterns generated by a diffuser illuminated by partially coherent light," *Optica Acta Int. J. Opt.*, vol. 30, no. 9, pp. 1213–1216, Sep. 1983.
[32] W. Shang, W. Zhang, Z. Wu, Y. Li, and X. Kong, "SNR analysis with speckle noise in interferometry using monochromatic expanded source and fringe localization," *Opt. Commun.*, vol. 455, Jan. 2020, Art. no. 124451.
[33] G. Li, Y. Qiu, and H. Li, "Coherence theory of a laser beam passing through a moving diffuser," *Optics Exp.*, vol. 21, no. 11, pp. 13032–13039, 2013.
[34] B. Redding, M. A. Choma, and H. Cao, "Spatial coherence of random laser emission," *Opt. Lett.*, vol. 36, no. 17, pp. 3404–3406, 2011.
[35] Y. Yuan, Y. Bi, M. Y. Sun, D. Z. Wang, D. D. Wang, W. N. Gao, and S. Zhang, "Speckle evaluation in laser display: From speckle contrast to speckle influence degree," *Opt. Commun.*, vol. 454, Jan. 2020, Art. no. 124405.
[36] B. Shpilman and D. Abookasis, "Experimental results of imaging objects in turbid liquid integrating multiview circularly polarized speckle images and deconvolution method," *Opt. Laser Technol.*, vol. 121, Jan. 2020, Art. no. 105774.
[37] V. V. Tuchin, "Polarized light interaction with tissues," *J. Biomed. Opt.*, vol. 21, no. 7, p. 71114, 2016.
[38] J. W. Kim, H. Jang, G. H. Kim, S. W. Jun, and C. S. Kim, "Multi-spectral laser speckle contrast images using a wavelength-swept laser," *J. Biomed. Opt.*, vol. 24, no. 7, p. 76001, 2019.
[39] S. Thorpe and J. Gautrais, "Rank order coding," in *Computational Neuroscience*. Boston, MA, USA: Springer, 1998, pp. 113–118.
[40] J. Buijs, J. V. D. Gucht, and J. Sprakel, "Fourier transforms for fast and quantitative," *Laser Speckle Imaging. Sci. Rep.*, vol. 9, no. 1, pp. 1–9, 2019.
[41] W. Cheng, X. Zhu, X. Chen, M. Li, J. Lu, and P. Li, "Manhattan distance-based adaptive 3D transform-domain collaborative filtering for laser speckle imaging of blood flow," *IEEE Trans. Med. Imag.*, vol. 38, no. 7, pp. 1726–1735, Jul. 2019.
[42] L. Bento, F. Cunha, L. Távora, P. Assunção, S. Faria, and R. Fonseca-Pinto, "A methodology for laser speckle simulation in controlled dynamic processes," in *Proc. 42nd Int. Conv. Inf. Commun. Technol., Electron. Microelectron. (MIPRO)*, May 2019, pp. 326–329.
[43] Y. Pang, B. K. Chen, and W. Liu, "An investigation of plastic behaviour in cold-rolled aluminium alloy AA2024-T3 using laser speckle imaging sensor," *Int. J. Adv. Manuf. Technol.*, vol. 103, nos. 5–8, pp. 2707–2724, Aug. 2019.
[44] K. Zhou, C. Zhou, A. Sapre, J. H. Pavlock, A. Weaver, R. Muralidharan, J. Noble, J. Kovac, Z. Liu, and A. Ebrahimi, "Dynamic laser speckle imaging meets machine learning to enable rapid antibacterial susceptibility testing (DyRAST)," *ACS Sens.*, vol. 5, no. 10, pp. 3140–3149, Sep. 2020.
[45] S. Divitt, D. F. Gardner, and A. T. Watnik, "Imaging around corners in the mid-infrared using speckle correlations," *Opt. Exp.*, vol. 28, no. 8, p. 11051, 2020, doi: 10.1364/oe.388260.
[46] P. Saranya and S. Prabakaran, "Automatic detection of non-proliferative diabetic retinopathy in retinal fundus images using convolution neural network," *J. Ambient Intell. Humanized Comput.*, pp. 1–10, Sep. 2020, doi: 10.1007/s12652-020-02518-6.
[47] D. Y. Park and J. H. Park, "Hologram conversion for speckle free reconstruction using light field extraction and deep learning," *Opt. Exp.*, vol. 28, no. 4, pp. 5393–5409, 2020.
[48] H. Tang, D. Cho, D. Lew, T. Kim, and J. Park, "Rank order coding based spiking convolutional neural network architecture with energy-efficient membrane voltage updates," *Neurocomputing*, vol. 407, pp. 300–312, Sep. 2020, doi: 10.1016/j.neucom.2020.05.031.
[49] V. J. Uzzell and E. J. Chichilnisky, "Precision of spike trains in primate retinal ganglion cells," *J. Neurophysiol.*, vol. 92, no. 2, pp. 780–789, Aug. 2004.
[50] T. Gollisch and M. Meister, "Rapid neural coding in the retina with relative spike latencies," *Science* vol. 319, no. 5866, pp. 1108–1111, 2008.
[51] G. Portelli, J. M. Barrett, G. Hilgen, T. Masquelier, A. Maccione, S. D. Marco, L. Berdondini, P. Kornprobst, and E. Sernagor, "Rank order coding: A retinal information decoding strategy revealed by large-scale multielectrode array retinal recordings," *J. Neurocomput.*, vol. 407, pp. 300–312 and 24, Sep. 2020.
[52] D. Liu and S. Yue, "Event-driven continuous STDP learning with deep structure for visual pattern recognition," *IEEE Trans. Cybern.*, vol. 49, no. 4, pp. 1377–1390, Apr. 2019.
[53] S. M. Bohte, J. N. Kok, and H. La Poutré, "Error-backpropagation in temporally encoded networks of spiking neurons," *Neurocomputing*, vol. 48, nos. 1–4, pp. 17–37, Oct. 2002.
[54] W. Hu, Y. Huang, L. Wei, F. Zhang, and H. Li, "Deep convolutional neural networks for hyperspectral image classification," *J. Sensors*, vol. 2015, pp. 1–12, Jul. 2015, Art. no. 258619, doi: 10.1155/2015/258619.
[55] A. Tavanaei and A. S. Maida, "Multi-layer unsupervised learning in a spiking convolutional neural network," in *Proc. Int. Joint Conf. Neural Netw. (IJCNN)*, May 2017, pp. 2023–2030.
[56] A. Tavanaei, M. Ghodrati, S. R. Kheradpisheh, T. Masquelier, and A. Maida, "Deep learning in spiking neural networks," *Neural Netw.*, vol. 111, pp. 47–63, Mar. 2019.
[57] S. R. Kheradpisheh, M. Ganjtabesh, S. J. Thorpe, and T. Masquelier, "STDP-based spiking deep convolutional neural networks for object recognition," *Neural Netw.*, vol. 99, pp. 56–67, Mar. 2018.
[58] X. Yang, Z. Zhang, W. Zhu, S. Yu, L. Liu, and N. Wu, "Deterministic conversion rule for CNNs to efficient spiking convolutional neural networks," *Sci. China Inf. Sci.*, vol. 63, no. 2, Feb. 2020, Art. no. 122402.
[59] D. C. Ciresan, U. Meier, J. Masci, L. M. Gambardella, and J. Schmidhuber, "Flexible, high performance convolutional neural networks for image classification," in *Proc. 22nd Int. Joint Conf. Artif. Intell.*, 2011, pp. 1237–1242.
[60] N. K. Kasabov, *Evolving Connectionist Systems: The Knowledge Engineering Approach*. London, U.K.: Springer-Verlag, 2007.
[61] S. G. Wysoski, L. Benuskova, and N. Kasabov, "On-line learning with structural adaptation in a network of spiking neurons for visual pattern recognition," in *Proc. Int. Conf. Artif. Neural Netw.* Berlin, Germany: Springer, 2006, pp. 61–70.
[62] J. L. Lobo, I. Laña, J. D. Ser, M. N. Bilbao, and N. Kasabov, "Evolving spiking neural networks for online learning over drifting data streams," *Neural Netw.*, vol. 108, pp. 1–19, Dec. 2018.
[63] O. A. Zoubi, A. Mayeli, M. Awad, and H. Refai, "Hierarchical fusion evolving spiking neural network for adaptive learning," in *Proc. IEEE 17th Int. Conf. Cognit. Informat. Cognit. Comput. (ICCI*CC)*, Jul. 2018, pp. 86–91.
[64] I. Laña, J. L. Lobo, E. Capecci, J. D. Ser, and N. Kasabov, "Adaptive long-term traffic state estimation with evolving spiking neural networks," *Transp. Res. C, Emerg. Technol.*, vol. 101, pp. 126–144, Apr. 2019.
[65] H. Qiu, M. Garratt, D. Howard, and S. Anavatti, "Evolving spiking neural networks for nonlinear control problems," in *Proc. IEEE Symp. Ser. Comput. Intell. (SSCI)*, Nov. 2018, pp. 1367–1373.
[66] S. Schliebs, M. Defoin-Platel, S. Worner, and N. Kasabov, "Integrated feature and parameter optimization for an evolving spiking neural network: Exploring heterogeneous probabilistic models," *Neural Netw.*, vol. 22, nos. 5–6, pp. 623–632, Jul. 2009.
[67] J. Gautrais and S. Thorpe, "Rate coding versus temporal order coding: A theoretical approach," *Biosystems*, vol. 48, nos. 1–3, pp. 57–65, Nov. 1998.
[68] S. Soltic and N. Kasabov, "Knowledge extraction from evolving spiking neural networks with rank order population coding," *Int. J. Neural Syst.*, vol. 20, no. 6, pp. 437–445, Dec. 2010.
[69] S. G. Wysoski, L. Benuskova, and N. Kasabov, "Fast and adaptive network of spiking neurons for multi-view visual pattern recognition," *Neurocomputing*, vol. 71, nos. 13–15, pp. 2563–2575, Aug. 2008.
[70] L. van der Maaten and G. Hinton, "Visualizing data using t-SNE," *J. Mach. Learn. Res.*, vol. 9, pp. 2579–2605, Nov. 2008.
[71] M. Yu, S. Zhang, L. Zhao, and G. Kuang, "Deep supervised t-SNE for SAR target recognition," in *Proc. 2nd Int. Conf. Frontiers Sensors Technol. (ICFST)*, Apr. 2017, pp. 265–269.
[72] L. Van Der Maaten, "Learning a parametric embedding by preserving local structure," in *Proc. Artif. Intell. Statist.*, 2009, pp. 384–391.
[73] E. Bolturk and C. Kahraman, "A novel interval-valued neutrosophic AHP with cosine similarity measure," *Soft Comput.*, vol. 22, no. 15, pp. 4941–4958, Aug. 2018, doi: 10.1007/s00500-018-3140-y.
[74] M. Abdel-Basset, M. Mohamed, M. Elhoseny, L. H. Son, F. Chiclana, and A. E.-N.-H. Zaied, "Cosine similarity measures of bipolar neutrosophic set for diagnosis of bipolar disorder diseases," *Artif. Intell. Med.*, vol. 101, Nov. 2019, Art. no. 101735, doi: 10.1016/j.artmed.2019.101735.
[75] D. Liu, X. Chen, and D. Peng, "Some cosine similarity measures and distance measures between q-rung orthopair fuzzy sets," *Int. J. Intell. Syst.*, vol. 34, no. 7, pp. 1572–1587, Jul. 2019.

[76] E. P. Chou and S.-M. Hsu, "Cosine similarity as a sample size-free measure to quantify phase clustering within a single neurophysiological signal," *J. Neurosci. Methods*, vol. 295, pp. 111–120, Feb. 2018, doi: 10.1016/j.jneumeth.2017.12.007.
[77] T. Thongtan and T. Phienthrakul, "Sentiment classification using document embeddings trained with cosine similarity," in *Proc. 57th Annu. Meeting Assoc. Comput. Linguistics Student Res. Workshop*, 2019, pp. 407–414.
[78] P. Saipech and P. Seresangtakul, "Automatic thai subjective examination using cosine similarity," in *Proc. 5th Int. Conf. Adv. Inform. Concept Theory Appl. (ICAICTA)*, Aug. 2018, pp. 214–218.
[79] M. Benard Magara, S. O. Ojo, and T. Zuva, "A comparative analysis of text similarity measures and algorithms in research paper recommender systems," in *Proc. Conf. Inf. Commun. Technol. Soc. (ICTAS)*, Mar. 2018, pp. 1–5.
[80] M. Farooq and A. Hafeez, "COVID-ResNet: A deep learning framework for screening of COVID19 from radiographs," *Comput. Vis. Pattern Recognit.*, Mar. 2020, *arXiv:2003.14395*. [Online]. Available: https://arxiv.org/abs/2003.14395
[81] B. Liu, Q. Liu, Z. Zhu, T. Zhang, and Y. Yang, "MSST-ResNet: Deep multi-scale spatiotemporal features for robust visual object tracking," *Knowl.-Based Syst.*, vol. 164, pp. 235–252, Jan. 2019.
[82] H. Li, X.-J. Wu, and T. S. Durrani, "Infrared and visible image fusion with ResNet and zero-phase component analysis," *Infr. Phys. Technol.*, vol. 102, Nov. 2019, Art. no. 103039, doi: 10.1016/j.infrared.2019.103039.
[83] I. M. Wismadi, D. C. Khrisne, and I. M. A. Suyadnya, "Detecting the ripeness of harvest-ready dragon fruit using smaller VGGNet-like network," *J. Electr., Electron. Informat.*, vol. 3, no. 2, p. 35, Jan. 2020, doi: 10.24843/jeei.2019.v03.i02.p01.
[84] D. C. Khrisne and I. M. A. Suyadnya, "Indonesian herbs and spices recognition using smaller VGGNet-like network," in *Proc. Int. Conf. Smart Green Technol. Electr. Inf. Syst. (ICSGTEIS)*, Oct. 2018, pp. 221–224.
[85] H. Jun, L. Shuai, S. Jinming, L. Yue, W. Jingwei, and J. Peng, "Facial expression recognition based on VGGNet convolutional neural network," in *Proc. Chin. Autom. Congr. (CAC)*, Nov. 2018, pp. 4146–4151.
[86] A. G. Howard, M. Zhu, B. Chen, D. Kalenichenko, W. Wang, T. Weyand, M. Andreetto, and H. Adam, "Mobilenets: Efficient convolutional neural networks for mobile vision applications," *Comput. Vis. Pattern Recognit.*, Apr. 2017, *arXiv:1704.04861*. [Online]. Available: https://arxiv.org/abs/1704.04861
[87] J. Li, Z. L. Yu, Z. Gu, H. Liu, and Y. Li, "Dilated-inception net: Multi-scale feature aggregation for cardiac right ventricle segmentation," *IEEE Trans. Biomed. Eng.*, vol. 66, no. 12, pp. 3499–3508, Dec. 2019.
[88] D. Das, K. C. Santosh, and U. Pal, "Truncated inception net: COVID-19 outbreak screening using chest X-rays," *Phys. Eng. Sci. Med.*, vol. 43, no. 3, pp. 915–925, Sep. 2020.
[89] E. Hershko, L. E. Weiss, T. Michaeli, and Y. Shechtman, "Multicolor localization microscopy and point-spread-function engineering by deep learning," *Opt. Exp.*, vol. 27, no. 5, p. 6158, 2019, doi: 10.1364/oe.27.006158.
[90] Y. Li, Y. Xue, and L. Tian, "Deep speckle correlation: A deep learning approach toward scalable imaging through scattering media," *Optica*, vol. 5, no. 10, pp. 1181–1190, 2018.
[91] P. Zelger, K. Kaser, B. Rossboth, L. Velas, G. J. Schütz, and A. Jesacher, "Three-dimensional localization microscopy using deep learning," *Opt. Exp.*, vol. 26, no. 25, p. 33166, 2018, doi: 10.1364/oe.26.033166.

ALI SYARIATI MOHD SALLEH received the B.Sc. degree in electrical engineering from Universiti Teknologi Mara, in 2009, and the M.Sc. degree in computer and microelectronics system from Universiti Teknologi Malaysia, in 2015. He had ten years of professional experience with electronic industries at Intel and held various positions ranging from Lead Senior Engineer to Research and Development Engineer. He currently holds several patents ranging from embedded systems, the IoT, and machine intelligence systems.

HAZA NUZLY ABDUL HAMED received the degree in information technology, majoring in artificial intelligence, from Universiti Utara Malaysia, the master's degree in computer science from Universiti Teknologi Malaysia (UTM), and the Ph.D. degree from the Auckland University of Technology, New Zealand. He is currently a Senior Lecturer with the School of Computing and a Founding Member of the Applied Industrial Analytics Research Group (ALIAS), Faculty of Engineering, UTM. He worked as a Web Programmer and System Analyst. His research interests include computational intelligence, evolutionary computation, deep learning, optimization, spatiotemporal data processing, and information system development.

MOHD ADHAM ISA received the bachelor's and master's degrees in computer science and the Ph.D. degree in software engineering from Universiti Teknologi Malaysia (UTM), Malaysia. He is currently the Head of the Software Engineering Research Group (SERG), UTM. His main research interests include software engineering, software quality, software testing, requirement engineering, and software project management. A major part of his research projects focuses on software quality assurance, real-time embedded systems, as well as the Internet of Things (IoT).

HABIBOLLAH HARON received the bachelor's degree in computer science from Universiti Teknologi Malaysia (UTM), the M.Sc. degree in computer technology in manufacture from the University of Sussex, U.K., and the Ph.D. degree from UTM. Previously, he was as the President of Qaiwan University (QU), Sulaymaniyah, Kurdistan-Iraq to ensure the success of QU-UTM Franchise. He is currently a Professor in applied computing with UTM. His research interests include optimization in various domains, such as medical problems, manufacturing, robotic, and image processing. He has also been appointed as a Project Leader for various research projects at university, national, and international level.